# Structural basis of meiotic chromosome synaptic elongation through hierarchical fibrous assembly of SYCE2-TEX12

**Authors**

James M. Dunce[2,3], Lucy J. Salmon[2], & Owen R. Davies[1,2]

**Affiliations**

[1]Institute of Cell Biology, University of Edinburgh, Michael Swann Building, Max Born Crescent, Edinburgh EH9 3BF.

[2]Biosciences Institute, Faculty of Medical Sciences, Newcastle University, Framlington Place, Newcastle upon Tyne NE2 4HH, UK.

[3]Current address: Department of Biochemistry, University of Cambridge, 80 Tennis Court Road, Old Addenbrookes Site, Cambridge CB2 1GA, UK.

**Author for Correspondence**

Owen Davies: owen.davies@ed.ac.uk

**Keywords**

Meiosis, chromosome structure, double-strand break, chiasmata, synaptonemal complex, SYCE2, TEX12, self-assembly, coiled-coil, small-angle X-ray scattering, biophysics, X-ray crystallography, intermediate filaments

**Abstract**

The supramolecular structure of the synaptonemal complex (SC) mediates homologous chromosome synapsis and facilitates the formation of genetic crossovers during meiosis. The mammalian SC is formed of eight coiled-coil proteins which interact in specific subcomplexes and self-assemble into distinct macromolecular arrays that fulfil specific aspects of the SC's dynamic functional architecture. Here, we report the structure of SC subcomplex SYCE2-TEX12 and its mechanism of self-assembly into fibres that define the SC's midline longitudinal structure. X-ray crystal structures, electron microscopy, biophysical and mutational analyses reveal that SYCE2-TEX12 is assembled from 2:2 complexes in which TEX12 chains are positioned at either end of a rod-like SYCE2 dimer. These molecular building-blocks assemble laterally into 4:4 complexes, and longitudinally into fibres of potentially limitless length, which acts as string-like threads that wind around one another in intertwined fibres of up to 40-nm in width and several micrometres in length. This hierarchical assembly mechanism is reminiscent of intermediate filament proteins and results in SYCE2-TEX12 fibres that can span the entire chromosome length, thereby providing the underpinning structural support for SC elongation during meiotic chromosome synapsis.

## Introduction

Meiosis, the specialised form of cell division in gametogenesis, involves an extraordinary chromosome choreography that is embodied by the unique chromosome architecture exhibited upon synapsis (Hunter, 2015, Zickler and Kleckner, 2015, Cahoon and Hawley, 2016). In this enigmatic state, pairs of homologous chromosomes are synapsed along their length and contain physical continuities between their DNA backbones at typically two sites of genetic crossover. Whilst seemingly static, the iconic appearance of synapsed chromosomes fully encapsulates the immense dynamics that were required to achieve synapsis and that are destined to occur following desynapsis (Zickler and Kleckner, 2015). These unique chromosomal structures and dynamics are essential for generating haploid oocytes and spermatozoa that form diploid zygotes upon fertilisation (Kouznetsova et al., 2011, de Vries et al., 2005, Yuan et al., 2002, Yuan et al., 2000), and thus are fundamental to understanding human fertility and the molecular causes of infertility, miscarriage and aneuploidy.

To achieve the dynamics of reductive division, meiotic chromosomes adopt distinctive structures in which their chromatin is looped around proteinaceous cores such that the linearity of their genetic sequence is projected onto linear axes (Kleckner, 2006). These linear chromosomal arrays become tethered to the nuclear envelope at both telomeric ends by the meiotic telomere complex, where they are subject to microtubule forces that drive their rapid movement throughout the nucleus (Lee et al., 2015, Shibuya et al., 2015, Dunce et al., 2018b). These rapid prophase movements are thought to facilitate inter-homologue recombination searches from the approximately 400 induced double strand breaks per cell that result in homologous chromosomes becoming paired and aligned through a series of recombination intermediates along their length (Lee et al., 2012, Wynne et al., 2012). It is at this stage that the homologues undergo synapsis through assembly of the synaptonemal complex (SC), a supramolecular protein structure that 'zips' together the homologous chromosome axis along their length (Cahoon and Hawley, 2016). It is within the three-dimensional context of the SC that recombination intermediates are resolved, with approximately 10% forming crossovers and 90%

undergoing non-crossover resolution (Baudat et al., 2013). The SC is then dissolved, leaving crossovers as the sole physical connections between homologues, allowing the cleavage of arm cohesins to trigger their segregation and the end of meiosis I (Zickler and Kleckner, 2015).

Meiotic synapsis by the SC was discovered in 1956 through the observation of the tripartite assembly of chromosomes in crayfish spermatocytes (Moses, 1956). Similar structures were subsequently observed in mammals, insects, plants and yeast, and it is now understood that chromosome synapsis by the SC is almost universal in meiotic organisms (Moses, 1968, Westergaard and von Wettstein, 1972). The tripartite SC structure consists of the two chromosome axes (known as lateral elements), which are separated by approximately 100 nm, and a midline central element that runs parallel to the chromosome axes (Moses, 1968, Westergaard and von Wettstein, 1972). These proteinaceous structures are held together by a series of interdigitated transverse filaments, which form the teeth of the metaphorical SC 'zipper' (Solari and Moses, 1973). Electron microscopy and super-resolution studies of the mammalian SC suggest the presence of longitudinal, transverse and vertical components within the central element, and indicate that the SC's cross-section is roughly square, with a depth of up to 100 nm (Schmekel et al., 1993, Schucker et al., 2015, Spindler et al., 2019). In accordance with the variation in length of human chromosomes, their synapsed states by the SC vary in length between 4-24 µm (Solari, 1980). The central element, lateral elements and transverse filaments of the SC combine in a supramolecular protein assembly that is continuous along synapsed chromosomes. Given these dimensions, and considering possible solvent contents of between 80% and 20%, we can estimate a molecular weight of between 1.6 GDa and 6.4 GDa per µm of SC length. Thus, the range of molecular weights of full human SCs must lie between the limits of 6.4 GDa and 154 GDa, placing them amongst the largest individual protein structures within a cell.

Over the last thirty years, the protein components of the mammalian SC have been identified and their roles within the SC have been defined by genetics and cell imaging. This has revealed that

transverse filaments are formed of SYCP1 molecules (Meuwissen et al., 1992, de Vries et al., 2005), which are oriented with their N- and C-termini located within the central and lateral elements, respectively, such that the length of two juxtaposed SYCP1 molecules dictates the 100 nm width of the SC (Schmekel et al., 1996, Liu et al., 1996, Schucker et al., 2015, Dunce et al., 2018a). The lateral elements contain SYCP2 and SYCP3 (Yuan et al., 2002, Yuan et al., 2000, Yang et al., 2006), whilst the central element is formed of SYCE1, SYCE2, SYCE3, TEX12 and SIX6OS1 (Costa et al., 2005, Schramm et al., 2011, Hamer et al., 2006, Gomez et al., 2016). All central region proteins, namely SYCP1 and the central element proteins, are essential for SC formation and meiosis, as their individual knockouts and targeted disruptions in mice lead to failure of synapsis and crossover formation, with meiotic failure and infertility (de Vries et al., 2005, Bolcun-Filas et al., 2009, Bolcun-Filas et al., 2007, Schramm et al., 2011, Hamer et al., 2008, Gomez et al., 2016). However, their knockout phenotypes reveal subtle differences in residual SC structure that provide important clues to their architectural roles. The SYCP1 knockout exhibits complete synaptic failure with lack of central element recruitment to chromosomes (de Vries et al., 2005). In SYCE1, SYCE3 and SIX6OS1 knockouts, there is patchy SYCP1 recruitment and associations between chromosomes, but without a tripartite SC (Bolcun-Filas et al., 2009, Schramm et al., 2011, Gomez et al., 2016). In contrast, SYCE2 and TEX12 knockouts demonstrate short stretches of tripartite structure, containing SYCP1, SYCE1, SYCE3 and SIX6OS1, but that are unable to extend along the chromosome axis (Bolcun-Filas et al., 2007, Hamer et al., 2008). These findings led to the proposal that SYCE1, SYCE3 and SIX6OS1 are initiation factors that provide short range stabilisation of nascent SYCP1 synapsis, with SYCE2 and TEX12 acting as elongation factors that underpin the SC's long-range growth by providing longitudinal structural support. This dichotomy is underpinned by biochemical findings that SYCE1 directly interacts with SYCE3 and SIX6OS1 (Lu et al., 2014, Sanchez-Saez et al., 2020), whilst SYCE2 and TEX12 exist in a seemingly constitutive complex (Davies et al., 2012).

In the last decade, the molecular underpinning of the SC has started to come into focus through analysis of SC proteins by structural biology (Syrjanen et al., 2014, Lu et al., 2014, Syrjanen et al., 2017,

Dunce et al., 2018a, Dunne and Davies, 2019a, Dunne and Davies, 2019b, West et al., 2019, Sanchez-Saez et al., 2020, Bollschweiler et al., 2019). An emerging theme is that SC proteins, which are almost universally coiled-coils, exist as defined building-blocks that can self-assemble into large molecular weight structures to provide the SC's distinct architectural elements. SYCP1 is a tetramer that assembles into a lattice-like array to fulfil the fundamental role of the SC in tethering chromosome axes (Dunce et al., 2018a). SYCP3 is a tetramer that assembles into paracrystalline fibres, which have been observed for the recombinant protein *in vitro* (Syrjanen et al., 2014, Bollschweiler et al., 2019), upon heterologous cellular expression (Yuan et al., 1998, Baier et al., 2007a, Baier et al., 2007b), and in the native mammalian SC (Ortiz et al., 2002). SYCP3 fibres separate DNA-binding sites by a 23 nm repeating unit along the longitudinal axis, which facilitates the compaction of chromatin loops within the meiotic chromosome axis (Syrjanen et al., 2014). Similarly, central element proteins SYCE2 and TEX12 exist in a 4:4 complex that assembles into fibres which vary in width between approximately 20-50 nm and extend up to 5 µm in length (Davies et al., 2012). Given the similarity between the appearance of SYCE2-TEX12 fibres and the SC's central element, which is approximately 35 nm wide and 4-24 µm in length, and the essential role of SYCE2 and TEX12 in SC elongation, the clear inference is that SYCE2-TEX12 fibres extend longitudinally within the central element to provide structural support for SC elongation along the chromosome length.

Here, we report the structural basis for the fibrous self-assembly of SYCE2-TEX12. We report the crystal structures of SYCE2-TEX12 in its building-block 2:2 and 4:4 complexes, which we combine with orthogonal biophysical studies by light and X-ray scattering, and visualisation by electron microscopy, to report its fibre assembly mechanism. In a manner reminiscent of intermediate filament proteins, SYCE2-TEX12's 2:2 building blocks undergo hierarchical assembly through lateral and longitudinal interfaces, through specific amino-acid contacts to achieve the formation of supramolecular fibrous arrays that underpin the SC's structure along the chromosome length.

## Results

### *SYCE2-TEX12 fibre assembly is mediated by TEX12's C-terminal tip*

A common feature of self-assembly by SC proteins SYCP1 and SYCP3 is the presence of short motifs at the ends of their α-helical cores that direct higher-order assembly (Syrjanen et al., 2014, Dunce et al., 2018a). In both cases, targeted disruption of these motifs block assembly and restrict proteins to their obligate 'building-block' structures. Could a similar phenomenon apply to SYCE2-TEX12 fibres? To test this, we analysed the oligomeric state and assembly of short deletions of the SYCE2-TEX12 core (amino-acids 57-165 and 49-123; Figure 1b) by size-exclusion chromatography multi-angle light scattering (SEC-MALS). Having confirmed that wild-type SYCE2-TEX12 core is a 4:4 complex that assembles into higher molecular weight species (Figure 1c,d), we identified that deletion of ten amino-acids at the C-terminal tip of TEX12 (ΔCtip, amino-acids 49-113; Figure 1b) restricted the SYCE2-TEX12 complex to a 2:2 stoichiometry and blocked its higher-order assembly (Figure 1c,d). Circular dichroism (CD) determined that wild-type and ΔCtip complexes have comparable α-helical contents (93% and 91%) and melting temperatures (71°C and 67°C) (Supplementary Figure 1a,b). Thus, the ΔCtip 2:2 complex may constitute a substructure of the wild-type 4:4 complex, and hence may represent its minimum building-block for assembly.

We find that full-length SYCE2-TEX12 has an increased propensity for assembling in solution, with SEC-MALS revealing its predominant formation of higher-order species, in addition to clearly discernible 4:4 and 2:2 complexes (Figure 1c,e). The presence of wild-type 2:2 complexes supports their putative role as the minimum obligate SYCE2-TEX12 structures, which may undergo hierarchical assembly into the observed 4:4 and higher-order species. In common with the core complex, deletion of TEX12's C-terminal tip restricted full-length SYCE2-TEX12 to a 2:2 complex and blocked higher-order assembly (Figure 1c,e). The α-helical structure and stability of the wild-type protein was retained in the ΔCtip complex (Supplementary Figure 1a,c). Thus, in a manner reminiscent of SYCP1 and SYCP3 (Syrjanen et al., 2014, Dunce et al., 2018a), deletion of a short motif at the C-terminal tip of TEX12 blocks higher-

order assembly and stabilises SYCE2-TEX12 in a 2:2 complex that likely represents the obligate 2:2 structure of the wild-type complex.

We next visualised SYCE2-TEX12 assembly by electron microscopy (Figure 2). This confirmed that core and full-length complexes assemble into morphologically similar fibres, which are typically positively-stained, vary in thickness up to a maximum of 50 nm and extend up to several micrometres in length (Figure 2a,d). Their distributions were determined through automated detection and measurement of fibres (Supplementary Figure 2), revealing that despite their similar lengths, mean fibre widths were slightly smaller for the full-length complex (12.8 ± 3.1 nm; Figure 2e,f) than its structural core (16.9 ± 4.1 nm; Figure 2b,c). This suggests that non-core sequences may provide additional interactions that confer stability to narrower core assemblies. In agreement with our SEC-MALS analysis, the TEX12 ΔCtip deletion blocked fibre formation of core and full-length complexes, as determined by manual inspection of micrographs (Figure 2a,d) and automated detection (Figure 2c,f). We conclude that TEX12's C-terminal tip is essential for assembly of SYCE2-TEX12 fibres, and its deletion stabilises the obligate 2:2 structure, providing a critical means for elucidating the fibre assembly mechanism.

***Crystal structure of SYCE2-TEX12 in a 2:2 complex***

The enhanced stability of the SYCE2-TEX12 ΔCtip core complex enabled the growth of protein crystals, which diffracted anisotropically to 2.42–3.36 Å resolution and enabled structure solution by molecular replacement of ideal helical fragments using *ARCIMBOLDO* (Table 1 and Supplementary Figure 3a). This revealed a 2:2 helical assembly in which an anti-parallel SYCE2 dimer spans the 14-nm length of the molecule and positions TEX12 chains in a staggered configuration (Figure 3a-c). The TEX12 chains are arranged with their N-termini towards the midline and their C-termini at either end of the molecule, immediately adjacent to the N- and C-termini of the SYCE2 antiparallel dimer (Figure 3a-c). The resultant 2:2 molecule has an unusual architecture in which a central four-helical bundle, formed of the SYCE2 dimer and overlapping N-terminal TEX12 chains, is flanked by three-helical bundles, each

formed of the SYCE2 dimer and a single C-terminal TEX12 chain (Figure 3a,d-f). Importantly, the C-terminal ends of SYCE2's core were not visible in electron density. Thus, deletion of TEX12's C-terminal tip corresponded with disorder of an analogous C-terminal sequence of the SYCE2 core (herein referred to as S2C; amino acids 155-165), such that the molecular ends of the 2:2 complex are formed of closely associated truncated C-termini of SYCE2 and TEX12 (Figure 3a,c).

Does the 2:2 crystal structure represent the solution state of SYCE2-TEX12 ΔCtip? Size-exclusion chromatography small-angle X-ray scattering (SEC-SAXS) of the ΔCtip core 2:2 complex revealed a real-space *P(r)* interatomic distance distribution and Guinier analysis indicative of a rod-like molecule with 19-nm length and 1.2-nm cross-sectional radius (Figure 3g,h, Table 2 and Supplementary Figure 3b,c). These dimensions match the length of the crystal structure with missing S2C ends modelled as ideal helices and its observed 2-nm width (Figure 3c and Supplementary Figure 3e). Further, the SAXS scattering curve was closely fitted by the crystal structure with modelled S2C helices and flexible N-termini ($\chi^2$ = 1.99; Figure 3g and Supplementary Figure 3e). We also analysed a ΔS2C/ΔCtip complex in which the C-termini of SYCE2 and TEX12 were deleted. SEC-MALS confirmed that the ΔS2C/ΔCtip core complex is predominantly 2:2 in solution (Supplementary Figure 3d). SEC-SAXS determined a rod-like molecule with 15-nm length and 1.2-nm cross-sectional radius, and *ab initio* envelope, matching the dimensions of the 2:2 crystal structure (Figure 3g-i, Table 2 and Supplementary Figure 3c). Further, the SAXS scattering curve was closely fitted by the crystal structure upon ideal helical modelling of the few missing C-terminal amino-acids ($\chi^2$ = 1.23; Figure 3g). We conclude that 2:2 crystal structure corresponds to the solution state of the ΔCtip core complex and hence represents the obligate 2:2 structure of SYCE2-TEX12 that provides the basis for its assembly.

***Crystal structure of SYCE2-TEX12 in a 4:4 assembly***

We obtained an alternative crystal form of the SYCE2-TEX12 ΔCtip core complex, which diffracted anisotropically to 3.33–6.00 Å resolution, and was solved by molecular replacement using a three-

helical bundle of the 2:2 structure as a search model (Table 1 and Supplementary Figure 4a). This revealed a 4:4 structure in which two 2:2 complexes interact laterally, through tessellation of S-shaped SYCE2 dimers, to create a molecule of the same length (14 nm) but twice as wide (4 nm) as individual 2:2 complexes (Figure 4a,b). The 2:2 crystal structure is largely retained by the two interacting 2:2 complexes (r.m.s. deviation = 1.91; Supplementary Figure 4b), which seamlessly generate an SYCE2 tetrameric core with staggered TEX12 chains arranged on opposing surfaces (Figure 4a). In common with the 2:2 structure, S2C sequences were missing from electron density, meaning that pairs of truncated SYCE2 and TEX12 C-termini are juxtaposed at either end of the 4:4 molecule (Figure 4c). The observed tessellation of 2:2 complexes provides an enticing mechanism for assembly of a 4:4 complex from structurally intact obligate 2:2 molecules, in agreement with our biochemical findings.

***The SYCE2-TEX12 4:4 complex is stabilised by TEX12 C-terminal tip interactions***

The 4:4 crystal structure lacks TEX12's C-terminal tip, which we know is required for 4:4 assembly in solution, suggesting that this conformation was supported by the crystal lattice. We reasoned that the same lateral 4:4 interface likely drives 4:4 assembly of the wild-type protein, which must be stabilised in solution by additional interactions of TEX12's Ctip. To test this, we introduced glutamate mutations of amino-acids H89 and Y115, which mediate the tessellating interaction of SYCE2 dimers within the 4:4 crystal structure whilst having no structural role within constituent 2:2 complexes (Figure 5a). Within the core complex, the H89E Y115E mutation partially blocked 4:4 assembly, restricting 60% of material to a 2:2 complex, despite the presence of Ctip sequences (Figure 5b). SEC-SAXS determined that the wild-type 4:4 complex has a 19-nm length and 1.9-nm cross-sectional radius (Figure 5c,d and Supplementary Figure 6b-d), matching the observed geometry of the 4:4 crystal structure in which the length of the 2:2 complex is retained and its width is doubled from 2 nm to 4 nm (Figure 4). Further, multi-phase SAXS *ab initio* modelling of the wild-type 4:4 structure placed ΔCtip 2:2 *ab initio* envelopes in parallel, consistent with their lateral tessellating interaction, with missing mass – corresponding to S2C and Ctip sequences – placed at either end of the molecule ($\chi^2$ = 1.69; Figure 5e). Thus, the lateral

tessellating interaction of 2:2 complexes within the 4:4 crystal structure describes the underlying architecture of the wild-type 4:4 assembly.

How does TEX12's Ctip stabilise the wild-type 4:4 complex? The location of pairs of truncated TEX12 and SYCE2 C-termini at either end of the 4:4 complex suggests that Ctip and S2C sequences could interact in four-helical structures that clamp together tessellated 2:2 structures. In support of this, deletion of SYCE2's S2C blocked 4:4 assembly and restricted the SYCE2-TEX12 core to a 2:2 complex (Supplementary Figure 5a), confirming that S2C and Ctip have equivalent roles in assembly. On the basis of heptad prediction, we modelled S2C-Ctip as a parallel heterodimeric coiled-coil, which docked seamlessly and in-phase with overlapping sequence of the 4:4 crystal structure to produce a model in which S2C-Ctip coiled-coils emanate from both ends of constituent 2:2 complexes (Supplementary Figure 5b). We then performed energy minimisation interspersed with geometry minimisation to allow closely associated pairs of S2C-Ctip dimers to interact with one another (Supplementary Figure 5b). This resulted in the formation of C-terminal bundles, consisting of parallel interactions between two S2C chains and two Ctip chains, which clamp together 2:2 complexes at either end of the lateral tessellating 4:4 interface (Figure 5f). The resultant 'clamped' 4:4 structure closed fitted the SAXS scattering curve of the wild-type 4:4 core complex upon flexible modelling of missing N-termini ($\chi^2$ = 2.47; Figure 5c). Thus, formation of S2C-Ctip C-terminal bundles provides a mechanism for clamping together laterally associated 2:2 complexes within the architecture of the wild-type 4:4 complex.

***Controlling the hierarchical assembly of SYCE2-TEX12***

Our model of the clamped 4:4 assembly allowed us to predict the sequence determinants of higher-order assembly by TEX12's Ctip. The C-terminal bundle includes TEX12 amino-acids L110, F114, I117 and L121 in its hydrophobic core and F102, V116 and F109 in solvent-exposed positions (Figure 6a,b). We thus predicted that these two groups of amino-acids are essential and dispensable for clamped 4:4 assembly, respectively. Accordingly, hydrophobic core mutation L110E F114E I117E L121E (LFIL)

restricted core and full-length SYCE2-TEX12 to 2:2 complexes and blocked fibrous assembly, thereby mimicking the Ctip deletion (Figure 6c-f). We similarly observed a restricted 2:2 complex upon analogous mutation of S2C hydrophobic core amino-acids V149, V153, V156 and L160 (Figure 6a and Supplementary Figure 6a). In contrast, surface mutation F102A V116A F109A (FVF) retained the 4:4 core complex, and wild-type pattern of full-length assembly in solution, but blocked higher-order assembly into fibres (Figures 2c,f and 6c-f). Importantly, SEC-SAXS confirmed that the 2:2 and 4:4 core complexes formed by LFIL and FVF mutants adopt the structures described for the ΔCtip and wild-type core complexes, respectively (Supplementary Figure 6b-g). We have thus identified separation-of-function mutations that block SYCE2-TEX12 in its obligate 2:2 structure and intermediate 4:4 assembly. The mimicry of Ctip deletion by LFIL mutation provides experimental validation for our proposed clamped 4:4 assembly model, whilst blockade of higher-order assembly by FVF mutation implicates these surface-exposed residues in the SYCE2-TEX12 fibre assembly mechanism.

***SYCE2-TEX12 forms 2-nm and 4-nm fibres***

How does TEX12's Ctip drive assembly of 4:4 complexes into SYCE2-TEX12 fibres? We obtained protein crystals of various SYCE2-TEX12 core constructs, including ΔCtip, which displayed a fibrous pattern of X-ray diffraction that is typical of the k-m-e-f family (keratin, myosin, epidermin, fibrinogen) of intermediate filament proteins (Figure 7a) (Squire, 1981, Kreplak et al., 2001, Er Rafik et al., 2004). This consists of a 5.1 Å meridional arc arising from the coiled-coil repeat, and 12 Å equatorial reflections, which correspond to inter-helical distances and are larger than the 9.8 Å distances of k-m-e-f proteins owing to the three-/four-helical bundle rather than dimeric coiled-coil structure. Upon rotation about the meridional axis, equatorial reflections resolved into regularly spaced reflections of 15-nm and 5-nm in parallel and perpendicular to the coiled-coil axis, respectively (Figure 7a). Correspondingly, the crystal lattice of the 4:4 structure is defined by 15-nm translations along the coiled-coil axis and 5-nm lateral spacings (Figure 7b). Thus, the crystal lattice fulfils the observed fibre parameters, with each linear array of 4:4 molecules representing a constituent fibre (Figure 7b).

The SYCE2-TEX12 4:4 crystal structure lacks the S2C and Ctip sequences required for fibre formation in solution. We reasoned that the crystal lattice must have stabilised fibre formation solely through lateral interactions, which would normally support and thicken constituent S2C-Ctip-assembled fibres, in which case it should be possible to rationalise S2C-Ctip's structural role within the crystalline fibrous array. We modelled S2C and Ctip as helical extensions of chains within 4:4 complexes *in situ*. This revealed that S2C and Ctip helices of juxtaposed 2:2 ends are ideally positioned to form anti-parallel four-helical bundles such that end-on 4:4 interactions are mediated by two stacked bundles (Figure 7c and Supplementary Figure 7a). Importantly, LFIL and S2C heptad residues are located within the hydrophobic core of S2C-Ctip bundles, whilst FVF residues are surface-exposed, suggesting roles in end-on and lateral fibre interactions, respectively, in agreement with their mutant phenotypes (Figure 7c). Our molecular model suggests that constituent SYCE2-TEX12 fibres could be 2-nm or 4-nm wide, formed from 2:2 or 4:4 building-blocks, and stabilised by individual S2C-Ctip bundles or the tessellating 4:4 interface with stacked bundles (Figure 7c). Further, it predicts that the lengths of constituent fibres are defined by a 20-nm initial subunit with 15-nm increments for additional subunits (Figure 7c).

We tested the fibre assembly model through SAXS analysis of the molecular length and cross-sectional radius of SYCE2-TEX12 core across its size-exclusion chromatography elution profile (Figure 7d). There was a stepwise increase in molecular length to 35 nm and 65 nm, with a progressive reduction in cross-sectional radius to 1.4 nm, at earlier elution points from the 20-nm (length) and 1.9-nm (radius) 4:4 complex (Figure 7d,e and Table 2). The cross-sectional radius is intermediate between 2:2 (1.2 nm) and 4:4 (1.9 nm) complexes, suggesting a mixture of 2:2 (2 nm width) and 4:4 (4 nm width) fibres. The 35-nm and 65-nm species correspond to the predicted lengths of end-on assemblies, and their SAXS scattering curves were fitted by modelled fibres of two 4:4 complexes (4 x 35 nm; $\chi^2$ = 1.22) and four 2:2 complexes (2 x 65 nm; $\chi^2$ = 1.09), respectively (Table 2 and Supplementary Figure 7b-e). Further, negatively-stained regions of electron micrographs allowed visualisation of the smallest SYCE2-TEX12

core assemblies (Figure 7f). We observed 2-nm and 4-nm structures that conform to the lengths of end-on assemblies, and automated analysis determined populations with mean fibre widths that correspond to 2:2 (2.3 ± 0.4 nm) and 4:4 (3.6 ± 1.0 nm) fibres (Figure 7f-h). Thus, experimental data support our molecular model of SYCE2-TEX12 assembly into 2-nm and 4-nm fibres.

***Hierarchical assembly of SYCE2-TEX12 fibres***

How do 2-nm and 4-nm fibres assemble into the thick fibres observed by electron microscopy and within the SC's central element? We visualised full-length SYCE2-TEX12 assemblies within negatively-stained regions of electron micrographs, revealing the presence of 2-nm (2.1 ± 0.8 nm) and 4-nm (4.1 ± 1.6 nm) fibres (Figure 8a-c). This confirmed its formation of the same constituent 2:2 and 4:4 fibres as the core complex, but with greater fibre length. We also observed 10-nm fibres (9.6 ± 2.4 nm), which frequently intertwined in bundles of up to 50 nm that accumulate stain and likely represent the positively-stained fibres that are ubiquitous in electron micrographs (Figure 8a-c). We conclude that SYCE2-TEX12 has a hierarchical assembly mechanism in which 2:2 and 4:4 molecules interact via S2C-Ctip bundles into 2-nm and 4-nm fibres, which thicken into 10-nm fibres through FVF residues and flanking termini, and are interwoven within thick bundled fibres (Figure 8d,e). The resultant rope-like fibres would provide longitudinal strength whilst permitting flexion and rotational motions necessary to constitute a structural backbone of the SC that spans the length of the meiotic chromosome axis.

**Discussion**

The inherent abilities of SYCE2-TEX12 and other SC components to undergo self-assembly *in vitro* substantially hamper our attempts at structure elucidation but also pose critical questions of their assembly mechanisms that require us to overcome these challenges of structural biology. Here, we utilised an approach that was previously successful for SC components SYCP1 and SYCE3 (Dunce et al., 2018a, Syrjanen et al., 2014), in which we identified a short truncation of TEX12's C-terminal tip that blocked assembly of SYCE2-TEX12 and restricted full-length and core complexes to 2:2 hetero-oligomers. This enabled the X-ray crystallographic structure solution of SYCE2-TEX12's minimum structural unit, a 2:2 complex, revealing an unusual three- and four-helical bundle fold in which TEX12 chains are positioned with their C-termini at either end of the rod-like structure of 20-nm length and 2-nm width. We propose that the 2:2 complex is SYCE2-TEX12's obligate structure that constitutes its minimum building-block for assembly into 4:4 complexes and fibres, and is comparable to the obligate tetramers of SYCP1 and SYCP3 that act as building-blocks for their respective assembly into lattice-like assays and paracrystalline fibres (Dunce et al., 2018a, Syrjanen et al., 2014, Bollschweiler et al., 2019).

Our crystal structure of SYCE2-TEX12 in a 4:4 assembly, combined with supporting biophysical solution and separation-of-function mutagenesis data, provide the basis for a model in which obligate 2:2 complexes assemble hierarchically into fibres. In this, assembly is achieved by specific interactions of well-defined amino-acids of the structural core that mediate lateral and longitudinal assembly, alongside poorly-defined interactions of the core and potentially unstructured terminal regions that enhance assembly. The 4:4 structure is formed through the lateral assembly of 2:2 complexes, achieving a structure of the same length (20 nm) but twice the width (4 nm). SYCE2-TEX12's obligate 2:2 and assembled 4:4 complexes both undergo longitudinal assembly through tip-to-tip interactions, which are potentially limitless and result in fibres of 2-nm and 4-nm width, respectively. If these core mechanisms are in place, the presence of unstructured termini further enhances assembly, enabling constituent fibres of approximately 10 nm in width to become intertwined, much in the way that

threads are wound into string, to form supramolecular fibres of approximately 50-nm width and many micrometres in length, corresponding to the known dimensions of the native SC's central element.

The three distinct molecular interfaces of SYCE2-TEX12 assembly explain the intriguing differences in the behaviour of full-length and core complexes in solution. Specifically, the full-length protein showed a high propensity for assembly in solution, forming a range of oligomers that include its minimum 2:2 complex. In contrast, the core structure appeared to be stabilised in its 4:4 complex, forming only tiny amounts of 2:2 complex and reduced assemblies. Further, electron microscopy indicated that full-length fibres are slightly thinner than core fibres. To explain these observations, we suggest that the unstructured termini of SYCE2 and TEX12 provide additional longitudinal stability to structures that are already assembled through core lateral and/or longitudinal interfaces, facilitating assembly elongation without extensive fibre thickening. To achieve similar assembly, core SYCE2-TEX12 forms thicker fibres through lateral associations, thereby increasing the number of longitudinal, end-on interactions acting in parallel to cooperatively stabilise fibre assembly. Thus, we propose that increased cooperativity of more end-on interactions in the thickened core fibres compensates for the lack of additional longitudinal strength that is provided by non-core amino-acid interactions within full-length fibres. Further, whilst unstructured termini favour assembly, they may also stabilise a single 2:2 complex by acting in 'cis' through termini binding to their own structural core. Thus, the core complex may represent an intriguingly restricted form of SYCE2-TEX12 in which the absence of unstructured termini reduces the propensity for assembly into higher-order fibres, whilst also reducing the stability in solution of the obligate 2:2 complex, resulting in its apparent stabilisation within a 4:4 complex that actually represents SYCE2-TEX12's partially assembled state.

It is apparent that our crystal structures and resultant models of the SYCE2-TEX12 4:4 complex and fibre assembly differ subtly but significantly from the model that we proposed almost a decade ago (Davies et al., 2012). Our previous model was based solely on the interaction ability and oligomeric

state of truncated proteins, in absence of high-resolution and solution structural data. It successfully predicted several important aspects of SYCE2-TEX12 structure, such as the parallel arrangement of elongated SYCE2 chains and a dominant interaction between SYCE2 N-termini and TEX12 C-termini within the 4:4 complex (Davies et al., 2012). However, a notable difference is that our previous model was built on the assumption of constituent TEX12 dimers, owing to their behaviour as such in solution, which we now know represents an entirely distinct structural and functional form of TEX12 (Sandhu et al., 2019). This led to the incorrect placement of TEX12 dimers flanking an SYCE2 core rather than intertwined within the hetero-octamer, and the prediction that the over-estimated 40-nm length of a heteroctamer could account for the width of the SYCE2-TEX12 fibres. In contrast, we have now determined that individual molecules of 20-nm length are arranged longitudinally in fibres. Our previous model was critical in designing mutations and experiments that ultimately resulted in the high-resolution structures presented herein. Nevertheless, this highlights the continued need for high-resolution experimental structure determination, particularly in the case of coiled-coil and hetero-oligomeric structures, which remain beyond the reaches of *in silico* structure prediction methods, despite advances in our understanding of protein folding and the increasing accuracy in predicting novel folds of monomers and homo-oligomers (Lepore et al., 2019, Callaway, 2020).

The ability of a small number of amino-acids within short C-terminal sequences to fully control the hierarchical assembly of SYCE2-TEX12 fibres provides clear parallels with our previous reports of SYCP1 and SYCP3 (Dunce et al., 2018a, Syrjanen et al., 2014). In all three cases, control sequences flank the obligate structural core, mediate longitudinal and lateral interactions between core structures, and their deletion or structure-directed mutation is sufficient to block or moderate assembly. Thus, despite their distinct supramolecular assemblies, these three SC components are built through similar principles of coiled-coil structure cores flanked by amino-acids that mediate higher-order assembly. This manner of assembly is also employed by intermediate filament proteins (Herrmann and Aebi, 2016). In keeping with this similarity, crystalline SYCE2-TEX12 assemblies exhibited X-ray diffraction

patterns consisting of 5.1 Å meridional arcs and 12 Å equatorial reflections. These X-ray diffraction properties are characteristic of the k-m-e-f family of intermediate filament proteins (encompassing keratin, myosin, epidermin and fibrinogen) (Squire, 1981, Kreplak et al., 2001, Er Rafik et al., 2004). The fibrous α-protein X-ray diffraction pattern is epitomised by Astbury's diffraction image of Mozart's hair (Astbury, 1960), and arises owing to a directional array of α-helices that are held in bundle structures to provide regular lateral spacing (Squire, 1981, Kreplak et al., 2001, Er Rafik et al., 2004). These shared features between SYCE2-TEX12 and k-m-e-f proteins raise the intriguing possibility that SYCE2-TEX12 fibres perform their essential function in chromosome synapsis by the SC by providing the level of fibrous strength that is renowned for molecules such as keratin.

How do SYCE2-TEX12 fibres function within the SC during meiosis? The knockout phenotypes of SC central element proteins resulted in their grouping into initiation factors (SYCE1, SYCE3 and SIX6OS1) that are essential for the formation of any tripartite SC structure (Bolcun-Filas et al., 2009, Schramm et al., 2011, Gomez et al., 2016), and elongation factors (SYCE2-TEX12) that are essential for extension of the SC along the chromosome length (Bolcun-Filas et al., 2007, Hamer et al., 2008). These findings, alongside the co-localisation of SYCE2 and TEX12 within the native SC central element (Hamer et al., 2006), are fully explained by a constitutive SYCE2-TEX12 complex that mediates elongation of nascent SC structure through formation of fibres that act as the SC's backbone. Thus, the intermediate filament-like nature of SYCE2-TEX12 fibres provides longitudinal strength and a single longitudinal axis to underpin the generation of a single continuous SC from discrete inter-homologue recombination events. Similarly, SYCP1 and SYCP3 assemblies have defined roles in the physical tethering of axes and stabilising compacted looped chromatin structure, respectively (Dunce et al., 2018a, Syrjanen et al., 2017, Syrjanen et al., 2014, Bollschweiler et al., 2019). Thus, we conclude that the SC's subcomplexes and components, including SYCP1, SYCP3 and SYCE2-TEX12, form unique supramolecular assemblies which provide distinct functionalities that are combined in a modular manner through interactions with other SC proteins to achieve the enigmatic structural and functional roles of the SC in meiosis.

## Materials and Methods

### Recombinant protein expression and purification

Sequences corresponding to regions of human SYCE2 (full-length, 1-218; core, 57-165; ΔS2C, 57-154) and TEX12 (full-length, 1-123; ΔCtip, 1-113; core, 49-123; core ΔCtip, 49-113) were cloned into pRSF-Duet1 (Novagen®) expression vectors for expression as TEV-cleavable N-terminal MBP- and $His_6$-fusion proteins, respectively. Constructs were co-expressed in BL21 (DE3) cells (Novagen®), in 2xYT media, induced with 0.5 mM IPTG for 16 hours at 25°C. Cells were lysed by sonication in 20 mM Tris pH 8.0, 500 mM KCl, and fusion proteins were purified from clarified lysate through consecutive Ni-NTA (Qiagen), amylose (NEB) and HiTrap Q HP (GE Healthcare) ion exchange chromatography. Affinity tags were removed by incubation with TEV protease and cleaved samples were purified by HiTrap Q HP ion exchange chromatography and size exclusion chromatography (HiLoad™ 16/600 Superdex 200, GE Healthcare) in 20 mM Tris pH 8.0, 150 mM KCl, 2 mM DTT. Protein samples were concentrated using Pall Microsep™ Advance centrifugal devices, and were stored at -80˚C following flash-freezing in liquid nitrogen. Protein samples were analysed by SDS-PAGE with Coomassie staining, and concentrations were determined by UV spectroscopy using a Cary 60 UV spectrophotometer (Agilent) with extinction coefficients and molecular weights calculated by ProtParam (http://web.expasy.org/protparam/).

### Crystallisation and structure solution of the SYCE2-TEX12 core ΔCtip 2:2 complex

SYCE2-TEX12 core ΔCtip protein crystals were obtained through vapour diffusion in sitting drops, by mixing 100 nl of 33 mg/ml protein at with 100 nl of crystallisation solution (35 % MPD) and equilibrating at 20°C for 4 months. Crystals were cryo-cooled in liquid nitrogen. X-ray diffraction data were collected at 0.9786 Å, 100 K, as 2000 consecutive 0.10° frames of 0.010 s exposure on a Pilatus3 6M detector at beamline I24 of the Diamond Light Source synchrotron facility (Oxfordshire, UK). Data were indexed, integrated in *XDS* (Kabsch, 2010), scaled in *XSCALE* (Diederichs et al., 2003), and merged with anisotropic correction and cut-off level at a local I/σ(I) of 1.2 using the *STARANISO* server (Tickle et al., 2018). Crystals belong to monoclinic spacegroup $P2_1$ (cell dimensions a = 88.52 Å, b = 24.19 Å, c

= 88.48 Å, α = 90°, β = 115.7°, γ = 90°), with a 2:2 SYCE2-TEX12 heterotetramer in the asymmetric unit. Structure solution was achieved through fragment-based molecular replacement using *ARCIMBOLDO_LITE* (Rodriguez et al., 2009), in which ten helices of 18 amino acids were placed by *PHASER* (McCoy et al., 2007) and extended by tracing in *SHELXE* utilising its coiled-coil mode (Caballero et al., 2018). A correct solution was identified by a *SHELXE* correlation coefficient of 47.8%. Model building was performed through iterative re-building by *PHENIX Autobuild* (Adams et al., 2010) building in *COOT* (Emsley et al., 2010). The structure was refined using *PHENIX refine* (Adams et al., 2010), using isotropic atomic displacement parameters with one TLS group. The structure was refined against data to anisotropy-corrected data with resolution limits between 2.42 Å and 3.36 Å, to *R* and $R_{free}$ values of 0.2871 and 0.3296 respectively, with 100% of residues within the favoured regions of the Ramachandran plot (0 outliers), clashscore of 6.89 and overall *MolProbity* score of 1.38 (Chen et al., 2010).

**Crystallisation and structure solution of the SYCE2-TEX12 core ΔCtip 4:4 complex**

SYCE2-TEX12 core ΔCtip protein crystals were obtained through vapour diffusion in sitting drops, by mixing 100 nl of protein at 33 mg/ml with 100 nl of crystallisation solution (0.1 M sodium acetate, pH 4.0, 65 % MPD) and equilibrating at 20°C for 4 months. Crystals were cryo-cooled in liquid nitrogen. X-ray diffraction data were collected at 0.9688 Å, 100 K, as 2000 consecutive 0.10° frames of 0.020 s exposure on a Pilatus3 6M detector at beamline I24 of the Diamond Light Source synchrotron facility (Oxfordshire, UK). Data were processed using *AutoPROC* (Vonrhein et al., 2011), in which indexing, integration and scaling were performed by *XDS* (Kabsch, 2010) and *XSCALE* (Diederichs et al., 2003), and anisotropic correction with a local I/σ(I) cut-off of 1.2 was performed by *STARANISO* (Tickle et al., 2018). Crystals belong to orthorhombic spacegroup $P2_12_12$ (cell dimensions a = 42.67 Å, b = 59.68 Å, c = 156.49 Å, α = 90°, β = 90°, γ = 90°), with a 2:2 SYCE2-TEX12 heterotetramer in the asymmetric unit. Structure solution was achieved by molecular replacement using *PHASER* (McCoy et al., 2007), in which two copies of one end of the higher resolution SYCE2-TEX12 2:2 structure (PDB accession 6R17)

were placed in the asymmetric unit. The structure was completed through manual building in *COOT* (Emsley et al., 2010), with iterative refinement using *PHENIX refine* (Adams et al., 2010). The structure was refined against data to anisotropy-corrected data with resolution limits between 3.33 Å and 6.00 Å, to $R$ and $R_{free}$ values of 0.3266 and 0.3672 respectively, with 100% of residues within the favoured regions of the Ramachandran plot (0 outliers), clashscore of 3.48 and overall *MolProbity* score of 1.14 (Chen et al., 2010).

**Crystallisation and X-ray diffraction analysis of SYCE2-TEX12 core ΔCtip fibres**

SYCE2-TEX12 core ΔCtip protein crystals were obtained through vapour diffusion in hanging drops, by mixing 1 µl of protein at 17 mg/ml in buffer containing 20% glycerol with 1 µl of crystallisation solution (0.05 M caesium chloride, 01 M MES pH 6.5, 30% v/v Jeffamine M-600) and equilibrating at 20°C. Crystals were cryo-cooled in liquid nitrogen in crystallisation solution supplemented with 25% glycerol. X-ray diffraction data were collected at 0.9763 Å, 100 K, as individual 0.50° frames of 0.500 s exposure on a Pilatus3 6M detector at beamline I03 of the Diamond Light Source synchrotron facility (Oxfordshire, UK). Diffraction images were analysed using *Adxv*.

**Size-exclusion chromatography multi-angle light scattering (SEC-MALS)**

The absolute molecular masses of SYCE2-TEX12 complexes were determined by size-exclusion chromatography multi-angle light scattering (SEC-MALS). Protein samples at >1 mg/ml were loaded onto a Superdex™ 200 Increase 10/300 GL size exclusion chromatography column (GE Healthcare) in 20 mM Tris pH 8.0, 150 mM KCl, 2 mM DTT, at 0.5 ml/min using an ÄKTA™ Pure (GE Healthcare). The column outlet was fed into a DAWN® HELEOS™ II MALS detector (Wyatt Technology), followed by an Optilab® T-rEX™ differential refractometer (Wyatt Technology). Light scattering and differential refractive index data were collected and analysed using ASTRA® 6 software (Wyatt Technology). Molecular weights and estimated errors were calculated across eluted peaks by extrapolation from

Zimm plots using a dn/dc value of 0.1850 ml/g. SEC-MALS data are presented as differential refractive index (dRI) profiles, with fitted molecular weights ($M_W$) plotted across elution peaks.

**Circular dichroism (CD) spectroscopy**

Far UV circular dichroism (CD) spectroscopy data were collected on a Jasco J-810 spectropolarimeter (Institute for Cell and Molecular Biosciences, Newcastle University). CD spectra were recorded in 10mM $Na_2HPO_4$/ $NaH_2PO_4$ pH 7.5, at protein concentrations between 0.1-0.5 mg/ml, using a 0.2 mm pathlength quartz cuvette (Hellma), at 0.2 nm intervals between 260 and 185 nm at 4°C. Spectra were averaged across nine accumulations, corrected for buffer signal, smoothed and converted to mean residue ellipticity ([θ]) (x1000 deg.cm$^2$.dmol$^{-1}$.residue$^{-1}$). Deconvolution was performed using the CDSSTR algorithm of the Dichroweb server (http://dichroweb.cryst.bbk.ac.uk) (Sreerama and Woody, 2000, Whitmore and Wallace, 2008). CD thermal denaturation was performed in 20 mM Tris pH 8.0, 150 mM KCl, 2 mM DTT, at protein concentrations between 0.1-0.4 mg/ml, using a 1 mm pathlength quartz cuvette (Hellma). Data were recorded at 222 nm, between 5°C and 95°C, at 0.5°C intervals with ramping rate of 2°C per minute, and were converted to mean residue ellipticity ($[\theta_{222}]$) and plotted as % unfolded $([\theta]_{222,x}-[\theta]_{222,5})/([\theta]_{222,95}-[\theta]_{222,5})$. Melting temperatures (Tm) were estimated as the points at which samples are 50% unfolded.

**Electron Microscopy**

Electron microscopy (EM) was performed using FEI Philips CM100 and 120 kV Hitachi HT7800 transmission electron microscopes at the Electron Microscopy Research Services, Newcastle University. Protein samples at 0.005-3 mg/ml were applied to carbon-coated grids and negative staining was performed using 2% (weight/volume) uranyl acetate. Images were analysed in the Fiji distribution of ImageJ (Schindelin et al., 2012), by applying background correction and an FFT Bandpass filter, and measuring the number, mean width and length of fibres using the Ridge detection algorithm.

**Size-exclusion chromatography small-angle X-ray scattering (SEC-SAXS)**

SEC-SAXS experiments were performed at beamline B21 of the Diamond Light Source synchrotron facility (Oxfordshire, UK). Protein samples at concentrations >5 mg/ml were loaded onto a Superdex™ 200 Increase 10/300 GL size exclusion chromatography column (GE Healthcare) in 20 mM Tris pH 8.0, 150 mM KCl at 0.5 ml/min using an Agilent 1200 HPLC system. The column outlet was fed into the experimental cell, and SAXS data were recorded at 12.4 keV, detector distance 4.014 m, in 3.0 s frames. Data were subtracted and averaged, and analysed for Guinier region *Rg* and cross-sectional *Rg* (*Rc*) using ScÅtter 3.0 (http://www.bioisis.net), and *P(r)* distributions were fitted using *PRIMUS* (P.V.Konarev, 2003). *Ab initio* modelling was performed using *DAMMIF* (Franke and Svergun, 2009), in which 30 independent runs were performed in P1 or P22 symmetry and averaged. Multi-phase SAXS *ab initio* modelling was performed using *MONSA* (Svergun, 1999). Crystal structures and models were docked into *DAMFILT* and *MONSA* molecular envelopes using *SUPCOMB* (Kozin and Svergun, 2001), and were fitted to experimental data using *CRYSOL* (Svergun D.I., 1995) and *FoXS* (Schneidman-Duhovny et al., 2016), and flexible termini were modelled and fitted to experimental data using *CORAL* (Petoukhov et al., 2012).

**Structural modelling**

A heterodimeric coiled-coil of the SYCE2 and TEX12 C-termini, including their S2C and Ctip sequences (amino-acids 155-165 and 114-123, respectively) was modelled by CCbuilder 2.0 (Wood and Woolfson, 2018) and was docked onto the 2:2 and 4:4 crystal structures using PyMOL Molecular Graphics System, Version 2.3.2 Schrödinger, LLC. The 4:4 'closed' assembly was modelled by manual editing of C-terminal helical positioning in *COOT* (Emsley et al., 2010), followed by iterations of energy minimisation using Rosetta Relax (Nivon et al., 2013) interspersed with idealisation by PHENIX geometry minimisation (Adams et al., 2010). The 4:4 'open' fibre assembly was modelled by imposing the crystallographic translation symmetry of 156 Å along the long axis onto 4:4 complexes with

modelled C-terminal coiled-coils, followed by manual editing of C-terminal helical positioning in *COOT* (Emsley et al., 2010), with iterations of energy minimisation using Rosetta Relax (Nivon et al., 2013) interspersed with idealisation by PHENIX geometry minimisation (Adams et al., 2010).

**Protein sequence and structure analysis**

Multiple sequence alignments were generated using *Jalview* (Waterhouse et al., 2009), and molecular structure images were generated using the *PyMOL* Molecular Graphics System, Version 2.0.4 Schrödinger, LLC.

**Accession codes and data availability**

Crystallographic structure factors and atomic co-ordinates have been deposited in the Protein Data Bank (PDB) under accession numbers 6R17 and 6YQF. SAXS experimental data and models will be deposited in the Small Angle Scattering Biological Data Bank (SASBDB). All other data are available from the corresponding author upon reasonable request.

**Acknowledgements**

We thank Diamond Light Source and the staff of beamlines I03, I24 and B21 (proposals mx13587, mx18598, sm14435, sm15580, sm15897, sm15836 and sm21777). We thank A. Baslé and H. Waller for assistance with X-ray crystallographic and CD data collection. O.R.D. is a Wellcome Trust Senior Research Fellow (Grant Number 219413/Z/19/Z).

**Author contributions**

J.M.D. crystallised SYCE2-TEX12 2:2 and 4:4 complexes, and performed biophysical and electron microscopy experiments. L.J.S. collected initial biophysics data. O.R.D. solved the SYCE2-TEX12 crystal structures, analysed data, designed experiments and wrote the manuscript.

**Competing financial interests**

The authors declare no competing interests.

**References**


ADAMS, P. D., AFONINE, P. V., BUNKOCZI, G., CHEN, V. B., DAVIS, I. W., ECHOLS, N., HEADD, J. J., HUNG, L. W., KAPRAL, G. J., GROSSE-KUNSTLEVE, R. W., MCCOY, A. J., MORIARTY, N. W., OEFFNER, R., READ, R. J., RICHARDSON, D. C., RICHARDSON, J. S., TERWILLIGER, T. C. & ZWART, P. H. 2010. PHENIX: a comprehensive Python-based system for macromolecular structure solution. *Acta Crystallogr D Biol Crystallogr,* 66**,** 213-21.

ASTBURY, W. T. 1960. THE FUNDAMENTALS OF FIBRE RESEARCH: A PHYSICIST'S STORY. *Journal of the Textile Institute Proceedings,* 51**,** P515-P526.

BAIER, A., ALSHEIMER, M. & BENAVENTE, R. 2007a. Synaptonemal complex protein SYCP3: Conserved polymerization properties among vertebrates. *Biochim Biophys Acta,* 1774**,** 595-602.

BAIER, A., ALSHEIMER, M., VOLFF, J. N. & BENAVENTE, R. 2007b. Synaptonemal complex protein SYCP3 of the rat: evolutionarily conserved domains and the assembly of higher order structures. *Sex Dev,* 1**,** 161-8.

BAUDAT, F., IMAI, Y. & DE MASSY, B. 2013. Meiotic recombination in mammals: localization and regulation. *Nat Rev Genet,* 14**,** 794-806.

BOLCUN-FILAS, E., COSTA, Y., SPEED, R., TAGGART, M., BENAVENTE, R., DE ROOIJ, D. G. & COOKE, H. J. 2007. SYCE2 is required for synaptonemal complex assembly, double strand break repair, and homologous recombination. *Journal of Cell Biology,* 176**,** 741-747.

BOLCUN-FILAS, E., HALL, E., SPEED, R., TAGGART, M., GREY, C., DE MASSY, B., BENAVENTE, R. & COOKE, H. J. 2009. Mutation of the mouse Syce1 gene disrupts synapsis and suggests a link between synaptonemal complex structural components and DNA repair. *PLoS Genet,* 5**,** e1000393.

BOLLSCHWEILER, D., RADU, L., JOUDEH, L., PLITZKO, J. M., HENDERSON, R. M., MELA, I. & PELLEGRINI, L. 2019. Molecular architecture of the SYCP3 fibre and its interaction with DNA. *Open Biol,* 9**,** 190094.

CABALLERO, I., SAMMITO, M., MILLAN, C., LEBEDEV, A., SOLER, N. & USON, I. 2018. ARCIMBOLDO on coiled coils. *Acta Crystallogr D Struct Biol,* 74**,** 194-204.

CAHOON, C. K. & HAWLEY, R. S. 2016. Regulating the construction and demolition of the synaptonemal complex. *Nat Struct Mol Biol,* 23**,** 369-77.

CALLAWAY, E. 2020. 'It will change everything': DeepMind's AI makes gigantic leap in solving protein structures. *Nature,* 588**,** 203-204.

CHEN, V. B., ARENDALL, W. B., HEADD, J. J., KEEDY, D. A., IMMORMINO, R. M., KAPRAL, G. J., MURRAY, L. W., RICHARDSON, J. S. & RICHARDSON, D. C. 2010. MolProbity: all-atom structure validation for macromolecular crystallography. *Acta Crystallographica Section D-Biological Crystallography,* 66**,** 12-21.

COSTA, Y., SPEED, R., OLLINGER, R., ALSHEIMER, M., SEMPLE, C. A., GAUTIER, P., MARATOU, K., NOVAK, I., HOOG, C., BENAVENTE, R. & COOKE, H. J. 2005. Two novel proteins recruited by synaptonemal complex protein 1 (SYCP1) are at the centre of meiosis. *J Cell Sci,* 118**,** 2755-62.

DAVIES, O. R., MAMAN, J. D. & PELLEGRINI, L. 2012. Structural analysis of the human SYCE2–TEX12 complex provides molecular insights into synaptonemal complex assembly. *Open Biology,* 2**,** 120099.

DE VRIES, F. A., DE BOER, E., VAN DEN BOSCH, M., BAARENDS, W. M., OOMS, M., YUAN, L., LIU, J. G., VAN ZEELAND, A. A., HEYTING, C. & PASTINK, A. 2005. Mouse Sycp1 functions in synaptonemal complex assembly, meiotic recombination, and XY body formation. *Genes Dev,* 19**,** 1376-89.

DIEDERICHS, K., MCSWEENEY, S. & RAVELLI, R. B. 2003. Zero-dose extrapolation as part of macromolecular synchrotron data reduction. *Acta Crystallogr D Biol Crystallogr,* 59**,** 903-9.

DUNCE, J. M., DUNNE, O. M., RATCLIFF, M., MILLAN, C., MADGWICK, S., USON, I. & DAVIES, O. R. 2018a. Structural basis of meiotic chromosome synapsis through SYCP1 self-assembly. *Nat Struct Mol Biol,* 25**,** 557-569.

DUNCE, J. M., MILBURN, A. E., GURUSARAN, M., DA CRUZ, I., SEN, L. T., BENAVENTE, R. & DAVIES, O. R. 2018b. Structural basis of meiotic telomere attachment to the nuclear envelope by MAJIN-TERB2-TERB1. *Nat Commun,* 9**,** 5355.

DUNNE, O. M. & DAVIES, O. R. 2019a. A molecular model for self-assembly of the synaptonemal complex protein SYCE3. *J Biol Chem,* 294**,** 9260-9275.

DUNNE, O. M. & DAVIES, O. R. 2019b. Molecular structure of human synaptonemal complex protein SYCE1. *Chromosoma*.

EMSLEY, P., LOHKAMP, B., SCOTT, W. G. & COWTAN, K. 2010. Features and development of Coot. *Acta Crystallogr D Biol Crystallogr,* 66**,** 486-501.

ER RAFIK, M., DOUCET, J. & BRIKI, F. 2004. The intermediate filament architecture as determined by X-ray diffraction modeling of hard alpha-keratin. *Biophys J,* 86**,** 3893-904.

FRANKE, D. & SVERGUN, D. I. 2009. DAMMIF, a program for rapid ab-initio shape determination in small-angle scattering. *J Appl Crystallogr,* 42**,** 342-346.

GOMEZ, H. L., FELIPE-MEDINA, N., SANCHEZ-MARTIN, M., DAVIES, O. R., RAMOS, I., GARCIA-TUNON, I., DE ROOIJ, D. G., DERELI, I., TOTH, A., BARBERO, J. L., BENAVENTE, R., LLANO, E. & PENDAS, A. M. 2016. C14ORF39/SIX6OS1 is a constituent of the synaptonemal complex and is essential for mouse fertility. *Nat Commun,* 7**,** 13298.

HAMER, G., GELL, K., KOUZNETSOVA, A., NOVAK, I., BENAVENTE, R. & HOOG, C. 2006. Characterization of a novel meiosis-specific protein within the central element of the synaptonemal complex. *Journal of Cell Science,* 119**,** 4025-4032.

HAMER, G., WANG, H., BOLCUN-FILAS, E., COOKE, H. J., BENAVENTE, R. & HOOG, C. 2008. Progression of meiotic recombination requires structural maturation of the central element of the synaptonemal complex. *J Cell Sci,* 121**,** 2445-51.

HERRMANN, H. & AEBI, U. 2016. Intermediate Filaments: Structure and Assembly. *Cold Spring Harb Perspect Biol,* 8.

HUNTER, N. 2015. Meiotic Recombination: The Essence of Heredity. *Cold Spring Harb Perspect Biol,* 7.

KABSCH, W. 2010. Xds. *Acta Crystallogr D Biol Crystallogr,* 66**,** 125-32.

KLECKNER, N. 2006. Chiasma formation: chromatin/axis interplay and the role(s) of the synaptonemal complex. *Chromosoma,* 115**,** 175-94.

KOUZNETSOVA, A., BENAVENTE, R., PASTINK, A. & HOOG, C. 2011. Meiosis in mice without a synaptonemal complex. *PLoS One,* 6**,** e28255.

KOZIN, M. B. & SVERGUN, D. I. 2001. Automated matching of high- and low-resolution structural models. *Journal of Applied Crystallography,* 34**,** 33-41.

KREPLAK, L., DOUCET, J. & BRIKI, F. 2001. Unraveling double stranded alpha-helical coiled coils: an x-ray diffraction study on hard alpha-keratin fibers. *Biopolymers,* 58**,** 526-33.

LEE, C. Y., CONRAD, M. N. & DRESSER, M. E. 2012. Meiotic chromosome pairing is promoted by telomere-led chromosome movements independent of bouquet formation. *PLoS Genet,* 8**,** e1002730.

LEE, C. Y., HORN, H. F., STEWART, C. L., BURKE, B., BOLCUN-FILAS, E., SCHIMENTI, J. C., DRESSER, M. E. & PEZZA, R. J. 2015. Mechanism and regulation of rapid telomere prophase movements in mouse meiotic chromosomes. *Cell Rep,* 11**,** 551-63.

LEPORE, R., KRYSHTAFOVYCH, A., ALAHUHTA, M., VERASZTO, H. A., BOMBLE, Y. J., BUFTON, J. C., BULLOCK, A. N., CABA, C., CAO, H., DAVIES, O. R., DESFOSSES, A., DUNNE, M., FIDELIS, K., GOULDING, C. W., GURUSARAN, M., GUTSCHE, I., HARDING, C. J., HARTMANN, M. D., HAYES, C. S., JOACHIMIAK, A., LEIMAN, P. G., LOPPNAU, P., LOVERING, A. L., LUNIN, V. V., MICHALSKA, K., MIR-SANCHIS, I., MITRA, A. K., MOULT, J., PHILLIPS, G. N., JR., PINKAS, D. M., RICE, P. A., TONG, Y., TOPF, M., WALTON, J. D. & SCHWEDE, T. 2019. Target highlights in CASP13: Experimental target structures through the eyes of their authors. *Proteins,* 87**,** 1037-1057.

LIU, J. G., YUAN, L., BRUNDELL, E., BJORKROTH, B., DANEHOLT, B. & HOOG, C. 1996. Localization of the N-terminus of SCP1 to the central element of the synaptonemal complex and evidence for

direct interactions between the N-termini of SCP1 molecules organized head-to-head. *Exp Cell Res,* 226**,** 11-9.

LU, J., GU, Y., FENG, J., ZHOU, W., YANG, X. & SHEN, Y. 2014. Structural insight into the central element assembly of the synaptonemal complex. *Sci Rep,* 4**,** 7059.

MCCOY, A. J., GROSSE-KUNSTLEVE, R. W., ADAMS, P. D., WINN, M. D., STORONI, L. C. & READ, R. J. 2007. Phaser crystallographic software. *Journal of Applied Crystallography,* 40**,** 658-674.

MEUWISSEN, R. L., OFFENBERG, H. H., DIETRICH, A. J., RIESEWIJK, A., VAN IERSEL, M. & HEYTING, C. 1992. A coiled-coil related protein specific for synapsed regions of meiotic prophase chromosomes. *EMBO J,* 11**,** 5091-100.

MOSES, M. J. 1956. Chromosomal structures in crayfish spermatocytes. *J Biophys Biochem Cytol,* 2**,** 215-8.

MOSES, M. J. 1968. Synaptinemal Complex. *Annu Rev Genet* 2**,** 363-412.

NIVON, L. G., MORETTI, R. & BAKER, D. 2013. A Pareto-optimal refinement method for protein design scaffolds. *PLoS One,* 8**,** e59004.

ORTIZ, R., ECHEVERRIA, O. M., UBALDO, E., CARLOS, A., SCASSELLATI, C. & VAZQUEZ-NIN, G. H. 2002. Cytochemical study of the distribution of RNA and DNA in the synaptonemal complex of guinea-pig and rat spermatocytes. *Eur J Histochem,* 46**,** 133-42.

P.V.KONAREV, V. V. V., A.V.SOKOLOVA, M.H.J.KOCH, D. I. SVERGUN 2003. PRIMUS - a Windows-PC based system for small-angle scattering data analysis. *J Appl Cryst.,* 36**,** 1277-1282

PETOUKHOV, M. V., FRANKE, D., SHKUMATOV, A. V., TRIA, G., KIKHNEY, A. G., GAJDA, M., GORBA, C., MERTENS, H. D., KONAREV, P. V. & SVERGUN, D. I. 2012. New developments in the ATSAS program package for small-angle scattering data analysis. *J Appl Crystallogr,* 45**,** 342-350.

RODRIGUEZ, D. D., GROSSE, C., HIMMEL, S., GONZALEZ, C., DE ILARDUYA, I. M., BECKER, S., SHELDRICK, G. M. & USON, I. 2009. Crystallographic ab initio protein structure solution below atomic resolution. *Nature Methods,* 6**,** 651-U39.

SANCHEZ-SAEZ, F., GOMEZ, H. L., DUNNE, O. M., GALLEGO-PARAMO, C., FELIPE-MEDINA, N., SANCHEZ-MARTIN, M., LLANO, E., PENDAS, A. M. & DAVIES, O. R. 2020. Meiotic chromosome synapsis depends on multivalent SYCE1-SIX6OS1 interactions that are disrupted in cases of human infertility. *Sci Adv,* 6.

SANDHU, S., SALMON, L., HUNTER, J., WILSON, C., PERKINS, N., HUNTER, N., DAVIES, O. & MCCLURG, U. 2019. A pseudo-meiotic centrosomal function of TEX12 in cancer. *bioRxiv***,** 509869.

SCHINDELIN, J., ARGANDA-CARRERAS, I., FRISE, E., KAYNIG, V., LONGAIR, M., PIETZSCH, T., PREIBISCH, S., RUEDEN, C., SAALFELD, S., SCHMID, B., TINEVEZ, J. Y., WHITE, D. J., HARTENSTEIN, V., ELICEIRI, K., TOMANCAK, P. & CARDONA, A. 2012. Fiji: an open-source platform for biological-image analysis. *Nat Methods,* 9**,** 676-82.

SCHMEKEL, K., MEUWISSEN, R. L., DIETRICH, A. J., VINK, A. C., VAN MARLE, J., VAN VEEN, H. & HEYTING, C. 1996. Organization of SCP1 protein molecules within synaptonemal complexes of the rat. *Exp Cell Res,* 226**,** 20-30.

SCHMEKEL, K., SKOGLUND, U. & DANEHOLT, B. 1993. The three-dimensional structure of the central region in a synaptonemal complex: a comparison between rat and two insect species, Drosophila melanogaster and Blaps cribrosa. *Chromosoma,* 102**,** 682-92.

SCHNEIDMAN-DUHOVNY, D., HAMMEL, M., TAINER, J. A. & SALI, A. 2016. FoXS, FoXSDock and MultiFoXS: Single-state and multi-state structural modeling of proteins and their complexes based on SAXS profiles. *Nucleic Acids Res,* 44**,** W424-9.

SCHRAMM, S., FRAUNE, J., NAUMANN, R., HERNANDEZ-HERNANDEZ, A., HOOG, C., COOKE, H. J., ALSHEIMER, M. & BENAVENTE, R. 2011. A novel mouse synaptonemal complex protein is essential for loading of central element proteins, recombination, and fertility. *PLoS Genet,* 7**,** e1002088.

SCHUCKER, K., HOLM, T., FRANKE, C., SAUER, M. & BENAVENTE, R. 2015. Elucidation of synaptonemal complex organization by super-resolution imaging with isotropic resolution. *Proc Natl Acad Sci U S A,* 112**,** 2029-33.

SHIBUYA, H., HERNANDEZ-HERNANDEZ, A., MORIMOTO, A., NEGISHI, L., HOOG, C. & WATANABE, Y. 2015. MAJIN Links Telomeric DNA to the Nuclear Membrane by Exchanging Telomere Cap. *Cell,* 163**,** 1252-1266.

SOLARI, A. J. 1980. Synaptosomal complexes and associated structures in microspread human spermatocytes. *Chromosoma,* 81**,** 315-37.

SOLARI, A. J. & MOSES, M. J. 1973. The structure of the central region in the synaptonemal complexes of hamster and cricket spermatocytes. *J Cell Biol,* 56**,** 145-52.

SPINDLER, M. C., FILBECK, S., STIGLOHER, C. & BENAVENTE, R. 2019. Quantitative basis of meiotic chromosome synapsis analyzed by electron tomography. *Sci Rep,* 9**,** 16102.

SQUIRE, J. 1981. Protein Conformation and Characterization. *The Structural Basis of Muscular Contraction.* Boston, MA: Springer US.

SREERAMA, N. & WOODY, R. W. 2000. Estimation of protein secondary structure from circular dichroism spectra: comparison of CONTIN, SELCON, and CDSSTR methods with an expanded reference set. *Anal Biochem,* 287**,** 252-60.

SVERGUN D.I., B. C. K. M. H. J. 1995. CRYSOL – a Program to Evaluate X-ray Solution Scattering of Biological Macromolecules from Atomic Coordinates. *J. Appl. Cryst.,* 28**,** 768-773.

SVERGUN, D. I. 1999. Restoring low resolution structure of biological macromolecules from solution scattering using simulated annealing. *Biophys J,* 76**,** 2879-86.

SYRJANEN, J. L., HELLER, I., CANDELLI, A., DAVIES, O. R., PETERMAN, E. J., WUITE, G. J. & PELLEGRINI, L. 2017. Single-molecule observation of DNA compaction by meiotic protein SYCP3. *Elife,* 6.

SYRJANEN, J. L., PELLEGRINI, L. & DAVIES, O. R. 2014. A molecular model for the role of SYCP3 in meiotic chromosome organisation. *Elife,* 3.

TICKLE, I. J., FLENSBURG, C., KELLER, P., PACIOREK, W., SHARFF, A., VONRHEIN, C. & BRICOGNE, G. 2018. STARANISO (http://staraniso.globalphasing.org/cgi-bin/staraniso.cgi). *Cambridge, United Kingdom: Global Phasing Ltd.*

VONRHEIN, C., FLENSBURG, C., KELLER, P., SHARFF, A., SMART, O., PACIOREK, W., WOMACK, T. & BRICOGNE, G. 2011. Data processing and analysis with the autoPROC toolbox. *Acta Crystallogr D Biol Crystallogr,* 67**,** 293-302.

WATERHOUSE, A. M., PROCTER, J. B., MARTIN, D. M., CLAMP, M. & BARTON, G. J. 2009. Jalview Version 2--a multiple sequence alignment editor and analysis workbench. *Bioinformatics,* 25**,** 1189-91.

WEST, A. M., ROSENBERG, S. C., UR, S. N., LEHMER, M. K., YE, Q., HAGEMANN, G., CABALLERO, I., USON, I., MACQUEEN, A. J., HERZOG, F. & CORBETT, K. D. 2019. A conserved filamentous assembly underlies the structure of the meiotic chromosome axis. *Elife,* 8.

WESTERGAARD, M. & VON WETTSTEIN, D. 1972. The synaptinemal complex. *Annu Rev Genet,* 6**,** 71-110.

WHITMORE, L. & WALLACE, B. A. 2008. Protein secondary structure analyses from circular dichroism spectroscopy: methods and reference databases. *Biopolymers,* 89**,** 392-400.

WOOD, C. W. & WOOLFSON, D. N. 2018. CCBuilder 2.0: Powerful and accessible coiled-coil modeling. *Protein Sci,* 27**,** 103-111.

WYNNE, D. J., ROG, O., CARLTON, P. M. & DERNBURG, A. F. 2012. Dynein-dependent processive chromosome motions promote homologous pairing in C. elegans meiosis. *J Cell Biol,* 196**,** 47-64.

YANG, F., DE LA FUENTE, R., LEU, N. A., BAUMANN, C., MCLAUGHLIN, K. J. & WANG, P. J. 2006. Mouse SYCP2 is required for synaptonemal complex assembly and chromosomal synapsis during male meiosis. *J Cell Biol,* 173**,** 497-507.

YUAN, L., LIU, J. G., HOJA, M. R., WILBERTZ, J., NORDQVIST, K. & HOOG, C. 2002. Female germ cell aneuploidy and embryo death in mice lacking the meiosis-specific protein SCP3. *Science,* 296**,** 1115-8.

YUAN, L., LIU, J. G., ZHAO, J., BRUNDELL, E., DANEHOLT, B. & HOOG, C. 2000. The murine SCP3 gene is required for synaptonemal complex assembly, chromosome synapsis, and male fertility. *Mol Cell,* 5**,** 73-83.

YUAN, L., PELTTARI, J., BRUNDELL, E., BJORKROTH, B., ZHAO, J., LIU, J. G., BRISMAR, H., DANEHOLT, B. & HOOG, C. 1998. The synaptonemal complex protein SCP3 can form multistranded, cross-striated fibers in vivo. *J Cell Biol,* 142**,** 331-9.

ZICKLER, D. & KLECKNER, N. 2015. Recombination, Pairing, and Synapsis of Homologs during Meiosis. *Cold Spring Harb Perspect Biol,* 7.

**Table 1 Data collection, phasing and refinement statistics**

| | SYCE2-TEX12 ΔCtip 2:2 complex | SYCE2-TEX12 ΔCtip 4:4 assembly |
|---|---|---|
| **PDB accession** | 6R17 | 6YQF |
| | | |
| **Data collection** | | |
| Space group | $P2_1$ | $P2_12_12$ |
| Cell dimensions | | |
| *a*, *b*, *c* (Å) | 88.52, 24.19, 88.48 | 42.67, 59.68, 156.49 |
| α, β, γ (°) | 90, 115.737, 90 | 90, 90, 90 |
| Resolution (Å) | 79.74 – 2.42 (2.74 – 2.42)* | 47.45 – 3.33 (3.59 – 3.33) |
| Ellipsoidal resolution (Å) | 2.416 (0.780 a* - 0.625 c*) | 4.203 (a*) |
| (direction) | 2.795 (b*) | 3.710 (b*) |
| | 2.926 (0.491 a* + 0.871 c*) | 2.891 (c*) |
| $R_{meas}$ | 0.074 (1.293) | 0.246 (2.445) |
| $R_{pim}$ | 0.049 (0.914) | 0.098 (0.906) |
| $I / \sigma(I)$ | 10.2 (1.2) | 4.7 (1.0) |
| $CC_{1/2}$ | 0.999 (0.564) | 0.995 (0.516) |
| Completeness (spherical) (%) | 63.2 (10.5) | 64.8 (27.1) |
| Completeness (ellipsoidal) (%) | 86.2 (51.3) | 83.0 (82.7) |
| Redundancy | 3.4 (3.0) | 6.5 (7.2) |
| | | |
| **Refinement** | | |
| Resolution (Å) | 79.74 – 2.42 | 47.45 – 3.33 |
| No. reflections | 8497 | 4053 |
| $R_{work}$ / $R_{free}$ | 0.2871/0.3296 | 0.3266/0.3672 |
| No. atoms | 2536 | 2426 |
| Protein | 2526 | 2426 |
| Ligand/ion | 0 | 0 |
| Water | 10 | 0 |
| *B*-factors | 76.79 | 56.52 |
| Protein | 76.89 | 56.52 |
| Ligand/ion | N/A | N/A |
| Water | 53.44 | N/A |
| R.m.s. deviations | | |
| Bond lengths (Å) | 0.005 | 0.001 |
| Bond angles (°) | 0.788 | 0.272 |

*Values in parentheses are for highest-resolution shell.

**Table 2 Summary of SEC-SAXS data**

| SYCE2-TEX12 core | WT 4:4 | FVF 4:4 | LFIL 2:2 | ΔCtip 2:2 | ΔS2C ΔCtip 2:2 | WT 35 nm (l) fibre | WT 65 nm (l) fibre |
|---|---|---|---|---|---|---|---|
| **Guinier analysis** | | | | | | | |
| *I(0)* ($cm^{-1}$) | 0.019 ±1.4x$10^{-4}$ | 0.120 ±2.0x$10^{-4}$ | 0.019 ±4.5x$10^{-5}$ | 0.044 ±1.3x$10^{-4}$ | 0.021 ±5.0x$10^{-5}$ | 0.031 ±7.4x$10^{-4}$ | 0.042 ±6.2x$10^{-3}$ |
| *Rg* (Å) | 49 ±0.33 | 49 ±1.16 | 47 ±0.59 | 49 ±0.31 | 41 ±1.69 | 86 ±1.30 | 167 ±25.3 |
| *Rc* (Å) | 19.4 | 19.4 | 12.4 | 12.2 | 11.7 | 16.6 | 15.3 |
| $q_{min}$ ($Å^{-1}$) | 0.056 | 0.0036 | 0.0070 | 0.0039 | 0.0043 | 0.0042 | 0.0035 |
| ***P(r)* analysis** | | | | | | | |
| *I(0)* ($cm^{-1}$) | 0.019 ±3.2x$10^{-5}$ | 0.122 ±2.0x$10^{-4}$ | 0.020 ±3.9x$10^{-5}$ | 0.044 ±1.1x$10^{-4}$ | 0.021 ±6.2x$10^{-5}$ | 0.031 ±6.3x$10^{-4}$ | 0.045 ±1.5x$10^{-3}$ |
| *Rg* (Å) | 53 ±0.13 | 52 ±0.12 | 51 ±0.13 | 50 ±0.19 | 45 ±0.20 | 93 ±2.05 | 183 ±3.9 |
| $D_{max}$ (Å) | 190 | 188 | 180 | 185 | 154 | 350 | 650 |
| Porod volume ($Å^3$) | 138000 | 141000 | 86000 | 78400 | 65000 | 268000 | 264000 |
| MW from Porod volume (kDa) | 82 | 83 | 50 | 46 | 38 | 158 | 155 |
| $V_C$ ($Å^2$) | 701 | 708 | 498 | 487 | 428 | 1030 | 1785 |
| MW from $V_C$ (kDa) | 82 | 83 | 43 | 40 | 36 | 101 | 155 |
| ***DAMMIF ab initio* modelling *(30 models)*** | | | | | | | |
| *Symmetry* | P22 | P22 | P1 | P1 | P1 | N/A | N/A |
| *NSD* mean and s.d. | 0.773 ±0.120 | 0.766 ±0.184 | 0.883 ±0.040 | 0.833 ±0.031 | 0.653 ±0.016 | N/A | N/A |
| $\chi^2$ (reference model) | 1.33 | 1.18 | 1.15 | 1.31 | 0.99 | N/A | N/A |
| ***MONSA* multi-phase *ab initio modelling*** | | | | | | | |
| *Symmetry* | P2 | N/A | N/A | N/A | P2 | N/A | N/A |
| $\chi^2$ | 1.69 | N/A | N/A | N/A | 0.95-0.96 | N/A | N/A |
| **Structural modelling** | | | | | | | |
| *CRYSOL:* Crystal structure ($\chi^2$) | 178 | 200 | 32.2 | 14.2 | 2.32 | N/A | N/A |
| *CRYSOL*: + modelled C-terminal coiled-coil ($\chi^2$) | 13.5 | 20.2 | 8.84 | 3.40 | 1.23 | N/A | N/A |
| *CORAL*: + modelled flexible N-termini ($\chi^2$) | 2.47 | 3.29 | 4.64 | 1.99 | N/A | N/A | N/A |
| *FoXS*: fibril model ($\chi^2$) | N/A | N/A | N/A | N/A | N/A | 1.22 | 1.09 |

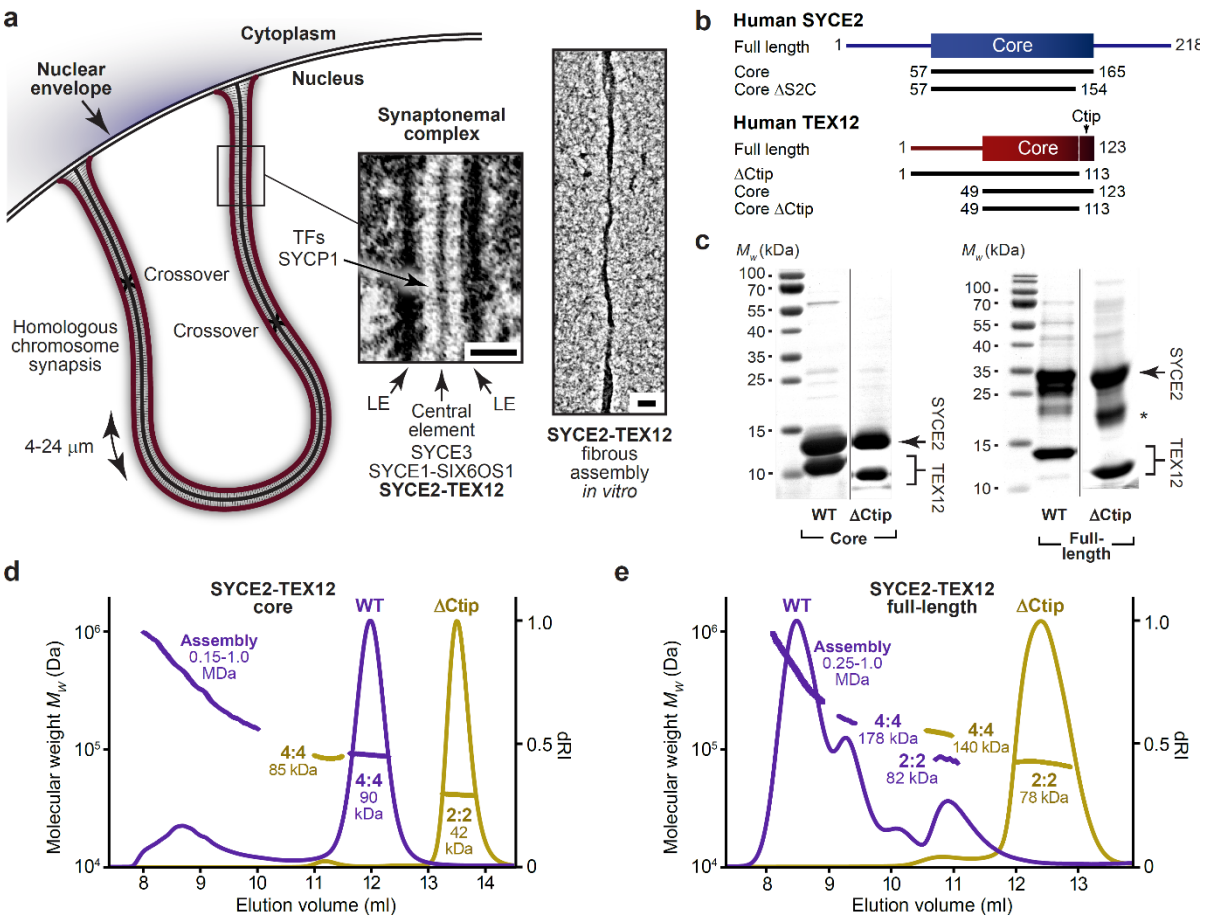


**Figure 1**

**SYCE2-TEX12 self-assembly is driven by the C-terminal tip of TEX12.**

(**a**) Schematic of the synaptonemal complex (SC) mediating full synapsis between homologous chromosomes that are physically tethered at both ends to the nuclear envelope. The SC has a tripartite structure of an electron-dense central element lying midway between chromosome-bound lateral elements (electron micrograph reproduced from Kouznetsova et al. (2011)). SC central element formation depends on an SYCE2-TEX12 complex that undergoes fibrous self-assembly *in vitro* (electron micrograph reproduced from Davies et al. (2012)). Scale bars, 100 nm. (**b**) Human SYCE2 and TEX12 sequences, depicting their α-helical structural cores and the principal constructs used in this study. (**c**) SDS-PAGE of purified SYCE2-TEX12 full-length and core complexes containing wild-type (WT) and ΔCtip TEX12 sequences. (**d-e**) SEC-MALS analysis of SYCE2-TEX12 (**d**) core and (**e**) full-length complexes in which differential refractive index (dRI) is shown with fitted molecular weights (*Mw*) plotted across elution peaks. (**d**) SYCE2-TEX12 core forms a 90 kDa 4:4 complex (75% of total mass; theoretical *Mw* -

89 kDa) and large molecular assemblies of up to 1.0 MDa (25%). Truncation of TEX12's C-terminal tip (ΔCtip) restricts SYCE2-TEX12 assembly to a 42 kDa 2:2 complex (98%; theoretical - 42 kDa) and 85 kDa 4:4 complex (2%; theoretical – 84 kDa). (**e**) SYCE2-TEX12 full-length forms an 82 kDa 2:2 complex (12%; theoretical – 78 kDa), 178 kDa 4:4 complex (18%; theoretical – 156 kDa) and large molecular assemblies of up to 1.0 MDa (70%). The TEX12 ΔCtip truncation restricts SYCE2-TEX12 assembly to a 78 kDa 2:2 complex (98%; theoretical – 76 kDa) and 140 kDa 4:4 complex (2%; theoretical – 151 kDa).

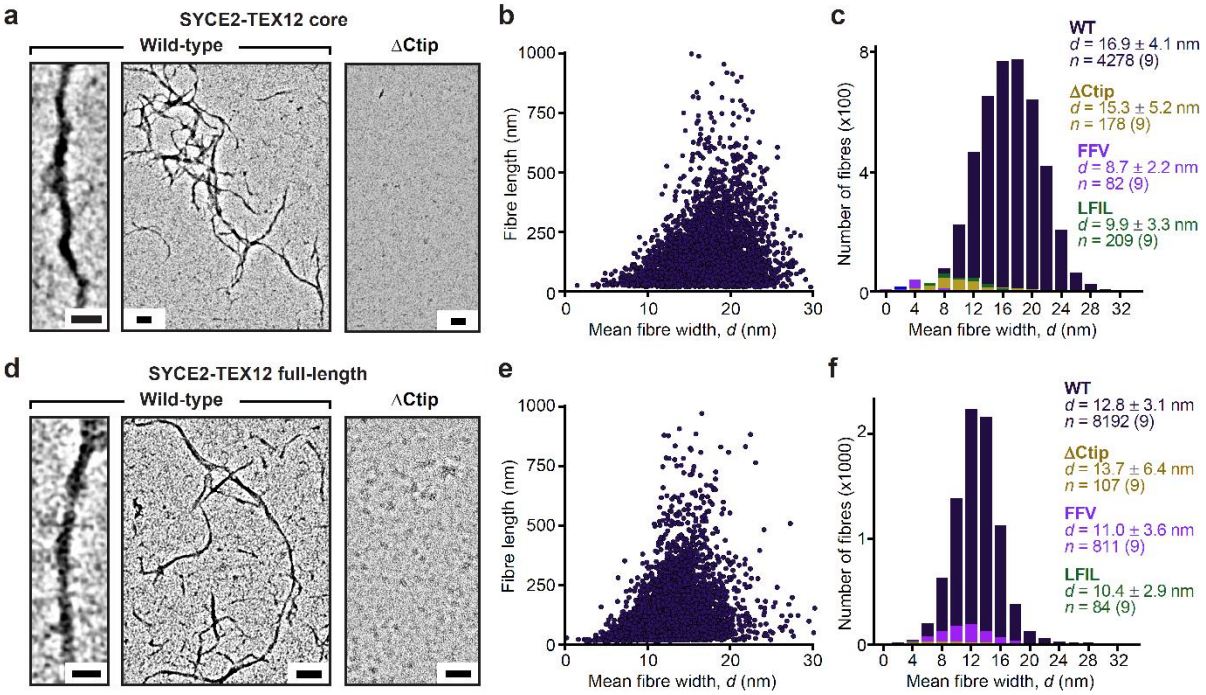


**Figure 2**

**Fibrous assembly of SYCE2-TEX12.**

(**a-f**) Electron microscopy of SYCE2-TEX12 (**a-c**) core and (**d-f**) wild-type. (**a**) Electron micrographs of SYCE2-TEX12 core wild-type and ΔCtip. Scale bars, 50 nm (left) and 100 nm (middle and right). (**b**) Scatter plot of mean fibre width (*d*, nm) against fibre length (nm) for wild-type SYCE2-TEX12 core. (**c**) Histograms of the number of fibres with mean widths within 2-nm bins for SYCE2-TEX12 core wild-type (dark blue), ΔCtip (yellow), FFV (F102A, F109A, V116A; light blue) and LFIL (L110E, F114E, I117E, L121E; green). The mean, standard deviation and number of fibres in each population is shown, each determined from nine micrographs. (**d**) Electron micrographs of SYCE2-TEX12 full-length wild-type and ΔCtip. Scale bars, 25 nm (left) and 100 nm (middle and right). (**e**) Scatter plot of mean fibre width (d, nm) against fibre length (nm) for wild-type SYCE2-TEX12. (**f**) Histograms of the number of fibres with mean widths within 2-nm bins for SYCE2-TEX12 full-length wild-type (dark blue), ΔCtip (yellow), FFV (F102A, F109A, V116A; light blue) and LFIL (L110E, F114E, I117E, L121E; green). The mean, standard deviation and number of fibres in each population is shown, each determined from nine micrographs.

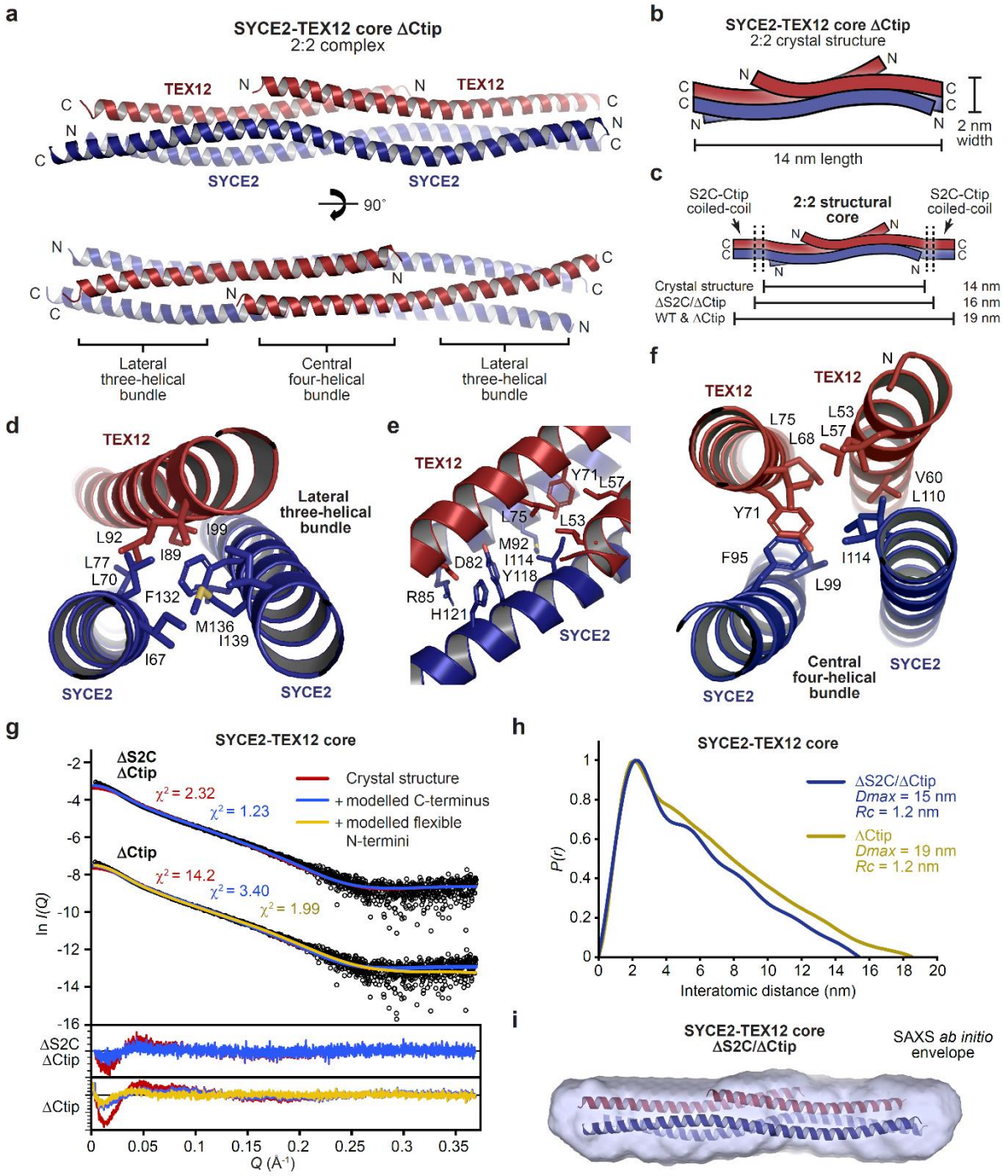


**Figure 3**

**Crystal structure of the SYCE2-TEX12 core 2:2 complex.**

(**a**) Crystal structure of SYCE2-TEX12 core ΔCtip as a 2:2 complex. The two TEX12 chains (red) are bound to either end of an SYCE2 anti-parallel dimer (blue), with their C-termini oriented externally and immediately adjacent to SYCE2's C-termini. The structure consists of a central four-helical bundle flanked by lateral three-helical bundles. (**b-c**) Schematics of the 2:2 crystal structure in which (**b**) the

orientation of SYCE2 and TEX12 chains are highlighted, and (**c**) their additional S2C and Ctip sequences are shown as C-terminal coiled-coils. The 2:2 structure has a width of 2 nm and a length of 14 nm, which is predicted to increase to 19 nm upon addition of S2C and/or Ctip sequences. (**d**) The lateral three-helical bundle consists of an anti-parallel arrangement of SYCE2 chains and a single TEX12 chain, with a hydrophobic core formed by the residues indicated. (**e**) The transition point between lateral three-helical bundle and central four-helical bundle. (**f**) The central four-helical bundle consists of an anti-parallel arrangement of two TEX12 and two SYCE2 chains, with a hydrophobic core formed by the residues indicated. (**g-i**) SEC-SAXS analysis of SYCE2-TEX12 core ΔS2C/ΔCtip and ΔCtip. (**g**) SAXS scattering data overlaid with the theoretical scattering curves of the 2:2 crystal structure (red), with modelled C-terminal coiled-coil and S2C helix (blue), and with flexibly modelled N-termini (yellow); $\chi^2$ values are indicated and residuals for each fit are shown (inset). (**h**) SAXS *P(r)* interatomic distance distributions of SYCE2-TEX12 core ΔS2C/ΔCtip and ΔCtip, showing maximum dimensions (*Dmax*) of 15 nm and 19 nm, respectively. Their cross-sectional radii (*Rc*) were determined as 1.2 nm. (**i**) SAXS *ab initio* model of SYCE2-TEX12 core ΔS2C/ΔCtip. A filtered averaged model from 30 independent DAMMIF runs is shown with the 2:2 crystal structure docked into the SAXS envelope.

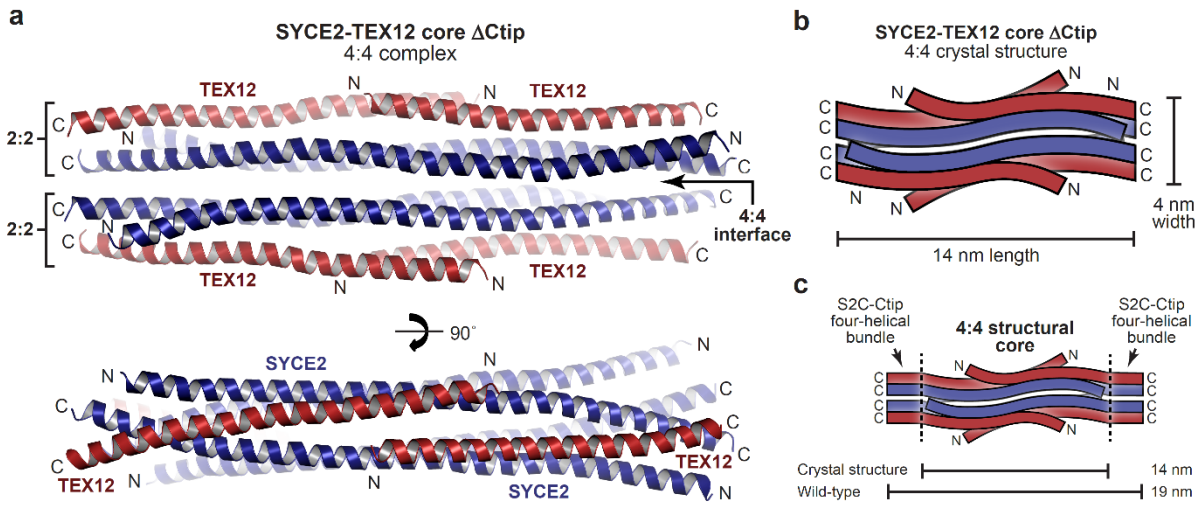


**Figure 4**

**Crystal structure of the SYCE2-TEX12 core 4:4 complex.**

(**a**) Crystal structure of SYCE2-TEX12 core ΔCtip as a 4:4 complex. The structure consists of two 2:2 complexes interacting side-by-side through tessellation of their undulating SYCE2 surfaces at a 4:4 interface. This results in a central core of four SYCE2 chains (blue) flanked by two TEX12 chains (red) on either side. (**b-c**) Schematics of the 4:4 crystal structure in which (**b**) the orientation of SYCE2 and TEX12 chains are highlighted, and (**c**) their additional S2C and Ctip sequences are shown as C-terminal four-helical bundles. The 4:4 structure has a width of 4 nm and a length of 14 nm, which is predicted to increase to 19 nm upon addition of S2C and Ctip sequences.

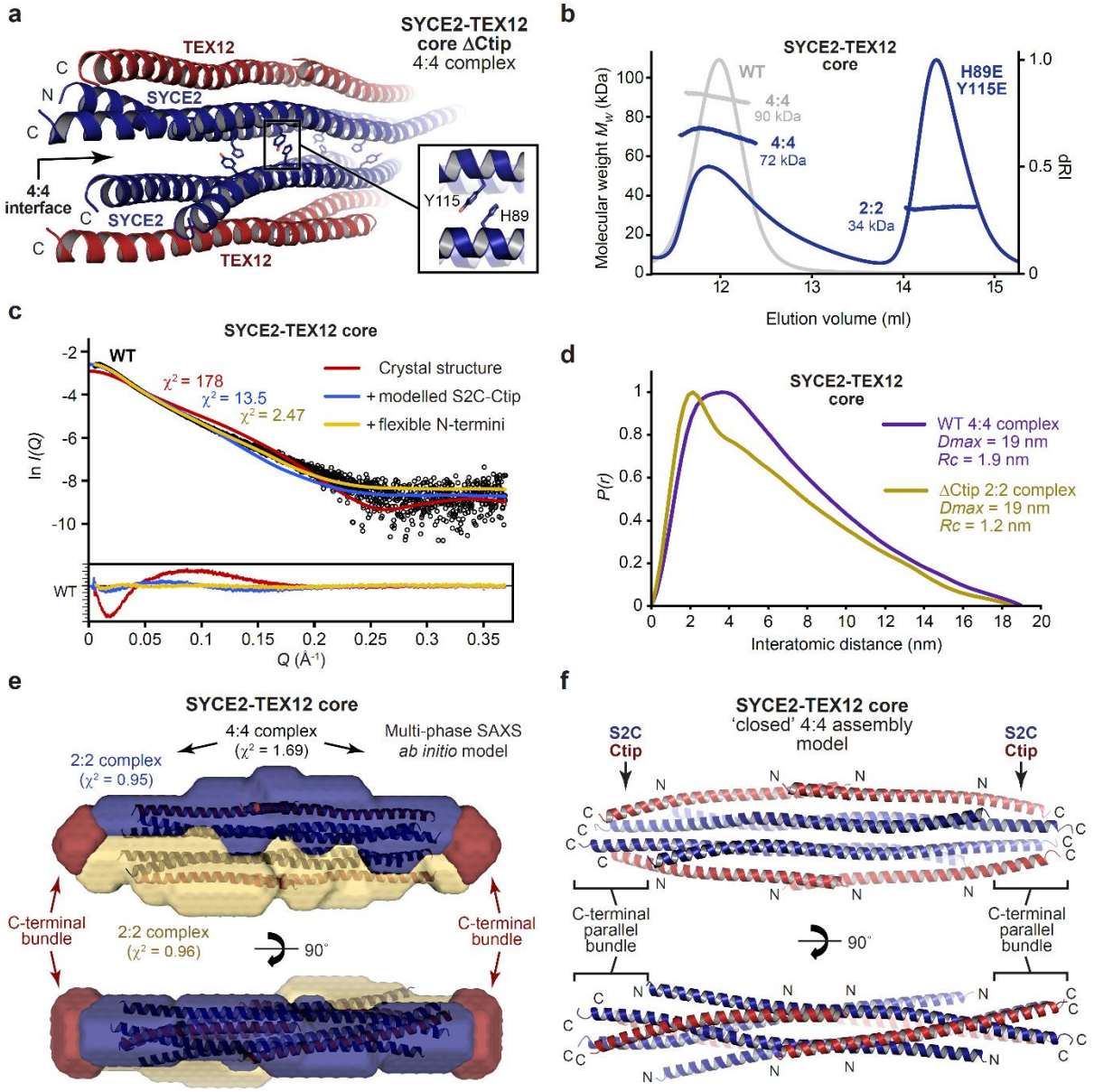


**Figure 5**

**A molecular model of the SYCE2-TEX12 core 'closed' 4:4 assembly.**

(**a**) Crystal structure of the SYCE2-TEX12 core ΔCtip 4:4 complex, highlighting interactions between SYCE2 residues H89 and Y115 at the 4:4 interface between juxtaposed 2:2 complexes. (**b**) SEC-MALS analysis of SYCE2-TEX12 core H89E/Y115E showing the formation of a 34 kDa 2:2 complex (60%; theoretical – 44 kDa) and 72 kDa 4:4 complex (40%; theoretical – 89 kDa). SYCE2-TEX12 core wild-type is shown in grey for comparison. (**c-e**) SEC-SAXS analysis of SYCE2-TEX12 core. (**c**) SAXS scattering data of SYCE2-TEX12 core overlaid with the theoretical scattering curves of the 4:4 crystal structure (red),

with modelled Ctip-S2C C-terminal bundles (blue), and with flexibly modelled N-termini (yellow); $\chi^2$ values are indicated and residuals for each fit are shown (inset). (**d**) SAXS *P(r)* interatomic distance distributions of SYCE2-TEX12 core wild-type and ΔCtip, showing maximum dimensions (*Dmax*) of 19 nm. Their cross-sectional radii (*Rc*) were determined as 1.9 nm and 1.2 nm, respectively. (**e**) Multi-phase SAXS *ab initio* (MONSA) model of the SYCE2-TEX12 core 4:4 complex (entire envelope; $\chi^2$=1.69), consisting of two SYCE2-TEX12 core ΔS2C/ΔCtip complexes (blue and yellow envelopes; $\chi^2$=0.95 and 0.96) and remaining mass corresponding to S2C-Ctip C-terminal bundles (red). (**f**) Theoretical model of the SYCE2-TEX12 core 'closed' 4:4 complex in which S2C-Ctip hetero-dimeric coiled-coils were docked onto the 4:4 crystal structure and assembled into C-terminal four-helical bundles through iterative energy minimisation and geometry idealisation.

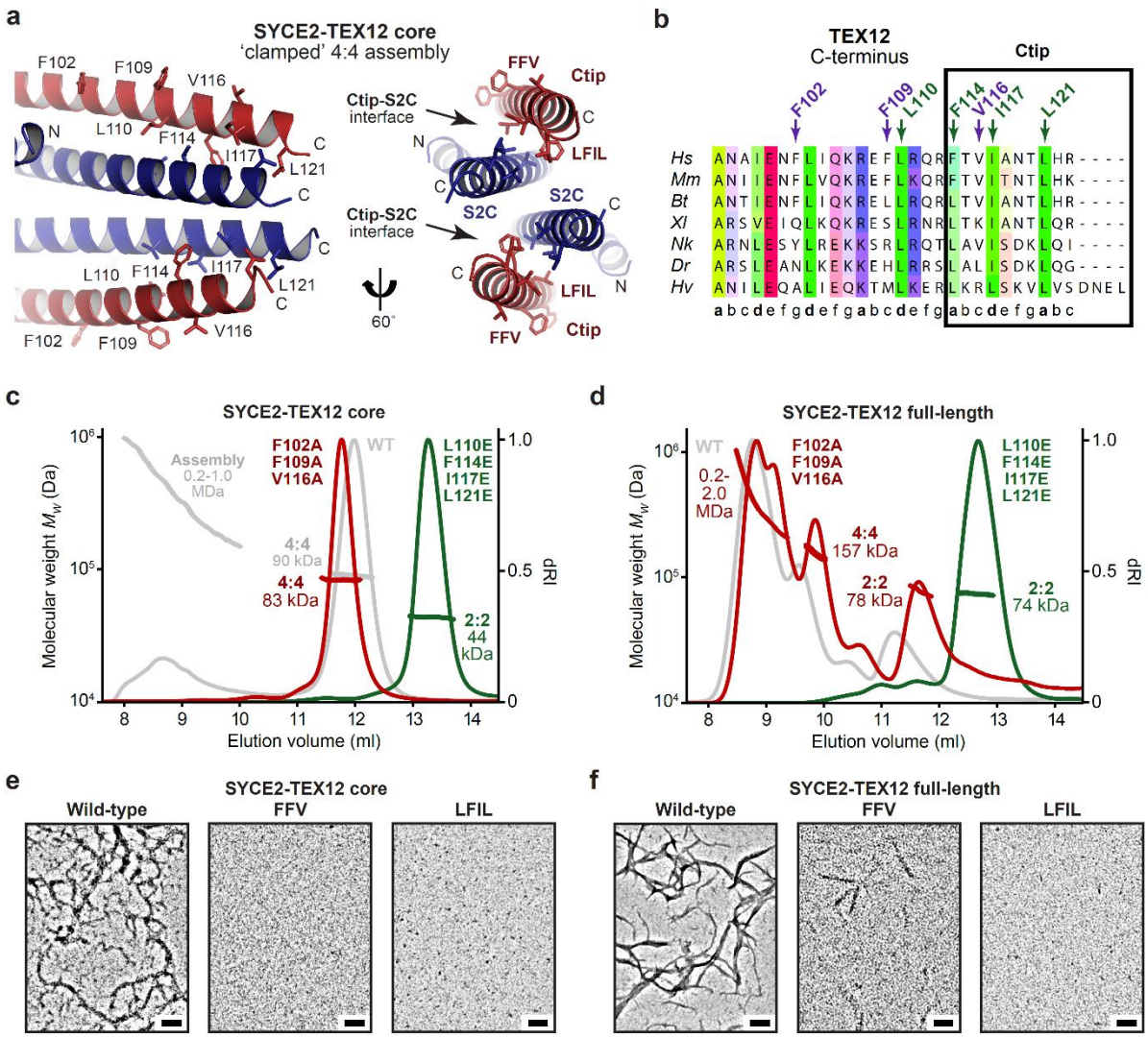


**Figure 6**

**Molecular determinants of SYCE2-TEX12 self-assembly by TEX12's C-terminal tip.**

(**a**) Molecular model of the SYCE2-TEX12 core ΔCtip 'closed' 4:4 assembly. The C-terminal bundle is formed of interactions between two S2C-Ctip coiled-coils, each of which involves heptad interactions between S2C residues V149, V153, V156 and L160, and Ctip residues L110, F114, I117 and L121 (LFIL), whilst F102, F109 and V116 (FFV) are solvent-exposed. (**b**) Multiple sequence alignment of the TEX12 C-terminus, highlighting the Ctip sequence and the presence of LFIL residues at heptad positions, and FFV residues at non-heptad positions. (**c-d**) SEC-MALS analysis of SYCE2-TEX12 (**c**) core and (**d**) full-length mutants F102A F109A V116A (FFV, red) and L110E F114E I117E L121E (LFIL, green), with wild-type shown in grey for comparison. (**c**) SYCE2-TEX12 core FFV forms an 83 kDa 4:4 complex (theoretical

– 88 kDa) with no higher-order assemblies, whilst LFIL forms a 44 kDa 2:2 complex (theoretical – 45 kDa). (**d**) SYCE2-TEX12 full-length FFV forms a 78 kDa 2:2 complex (15%; theoretical – 78 kDa), 155 kDa 4:4 complex (20%; theoretical – 156 kDa) and large molecular assemblies of up to 2.0 MDa (65%), whilst LFIL forms a 74 kDa 2:2 complex (theoretical – 78 kDa). (**e-f**) Electron microscopy of SYCE2-TEX12 (**e**) core and (**f**) full-length mutants. FFV inhibits SYCE2-TEX12 core assembly and restricts full-length to occasional fibres. LFIL inhibits SYCE2-TEX12 core and full-length fibrous assembly.

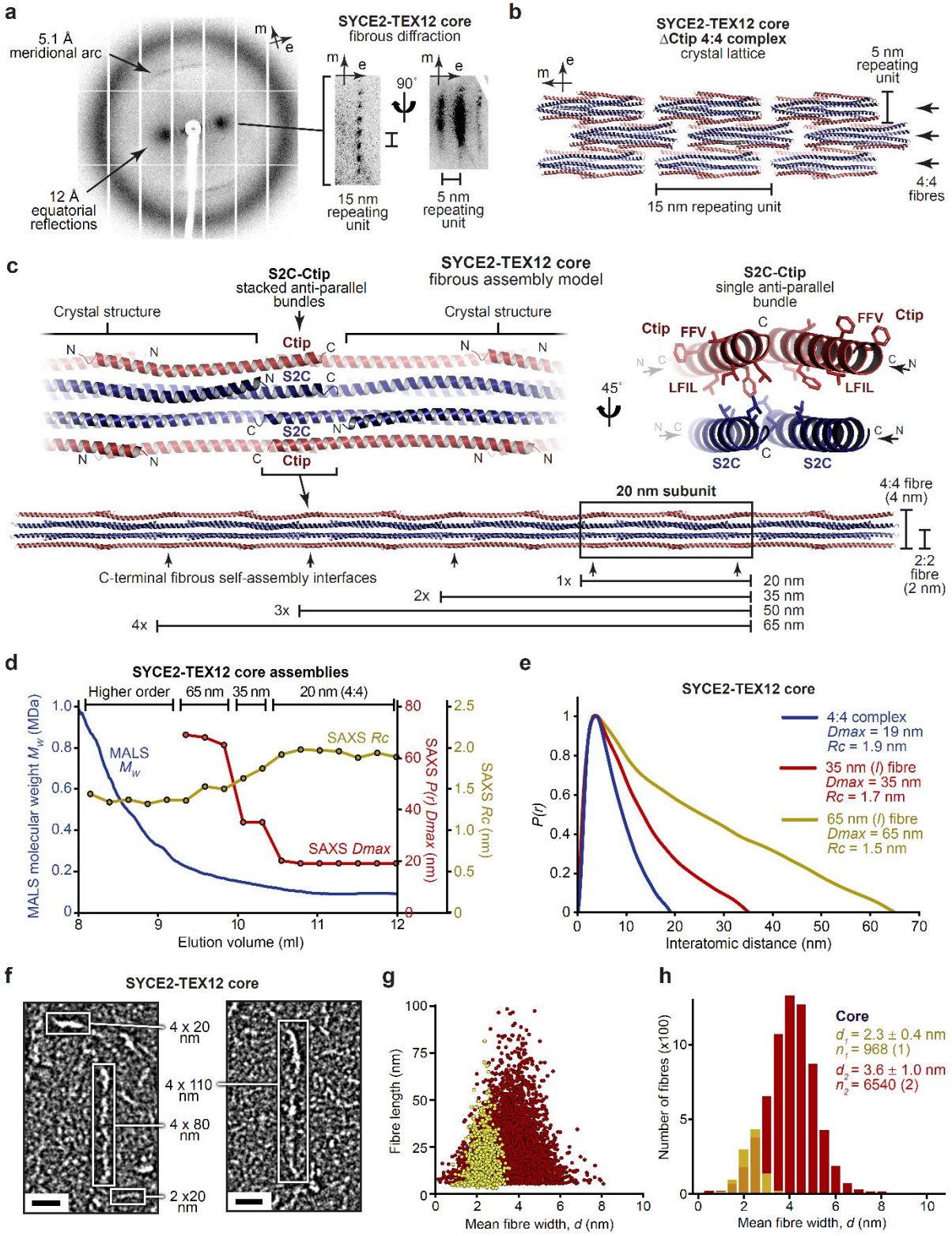


**Figure 7**

**A molecular model of the SYCE2-TEX12 core fibrous assembly.**

(**a**) X-ray diffraction pattern of SYCE2-TEX12 core ΔCtip crystals demonstrating 5.1 Å meridional arcs and 12 Å equatorial reflections, which resolve upon rotation about the meridional axis into

longitudinal and lateral spacings corresponding to 15 nm and 5 nm repeating units, respectively. (**b**) The SYCE2-TEX12 core ΔCtip 4:4 crystal lattice is formed of 15 nm translations along the meridional axis that generate 4:4 fibres, which associate laterally as 5 nm repeating units. (**c**) Theoretical model of SYCE2-TEX12 core fibrous assembly in which adjacent 4:4 complexes are translated by 15 nm and interact back-to-back through stacked S2C-Ctip anti-parallel four-helical bundles (left), of which each bundle contains a hydrophobic core of CtIP LFIL and S2C residues, with FFV residues remaining solvent-exposed (right). This assembly mechanism generates fibres of discrete lengths corresponding to the 20 nm initial subunit and integer multiples of the 15 nm repeating unit, with a width of 2 nm or 4nm if it is formed of 2:2 or 4:4 complexes, respectively. (**d-e**) SEC-SAXS analysis of SYCE2-TEX12 core assemblies. (**d**) SAXS *P(r)* maximum dimensions (*Dmax*, red), cross-sectional radii (*Rc*, yellow) and corresponding MALS molecular weights (blue) are shown across an elution peak; *Dmax* is not determined for higher-order species in which the Shannon limit is exceeded. (**e**) SAXS *P(r)* interatomic distance distributions of the SYCE2-TEX12 core 4:4 complex (blue) and its fibrous assemblies of lengths 35 nm (red) and 65 nm (yellow). (**f-h**) Electron microscopy of SYCE2-TEX12 core in which (**f**) electron micrographs reveal molecules of 2 x 20 nm, 4 x 20 nm, 4 x 80 nm and 4 x 110 nm (w x l). Scale bars, 20 nm. (**g**) Scatter plots of mean fibre width (*d*, nm) against fibre length (nm), and (**h**) histograms of the number of fibres with mean widths within 0.5-nm bins, for two distinct populations (2 nm, yellow; 4 nm, red). The mean, standard deviation and number of fibres in each population were determined from one and two micrographs, respectively.

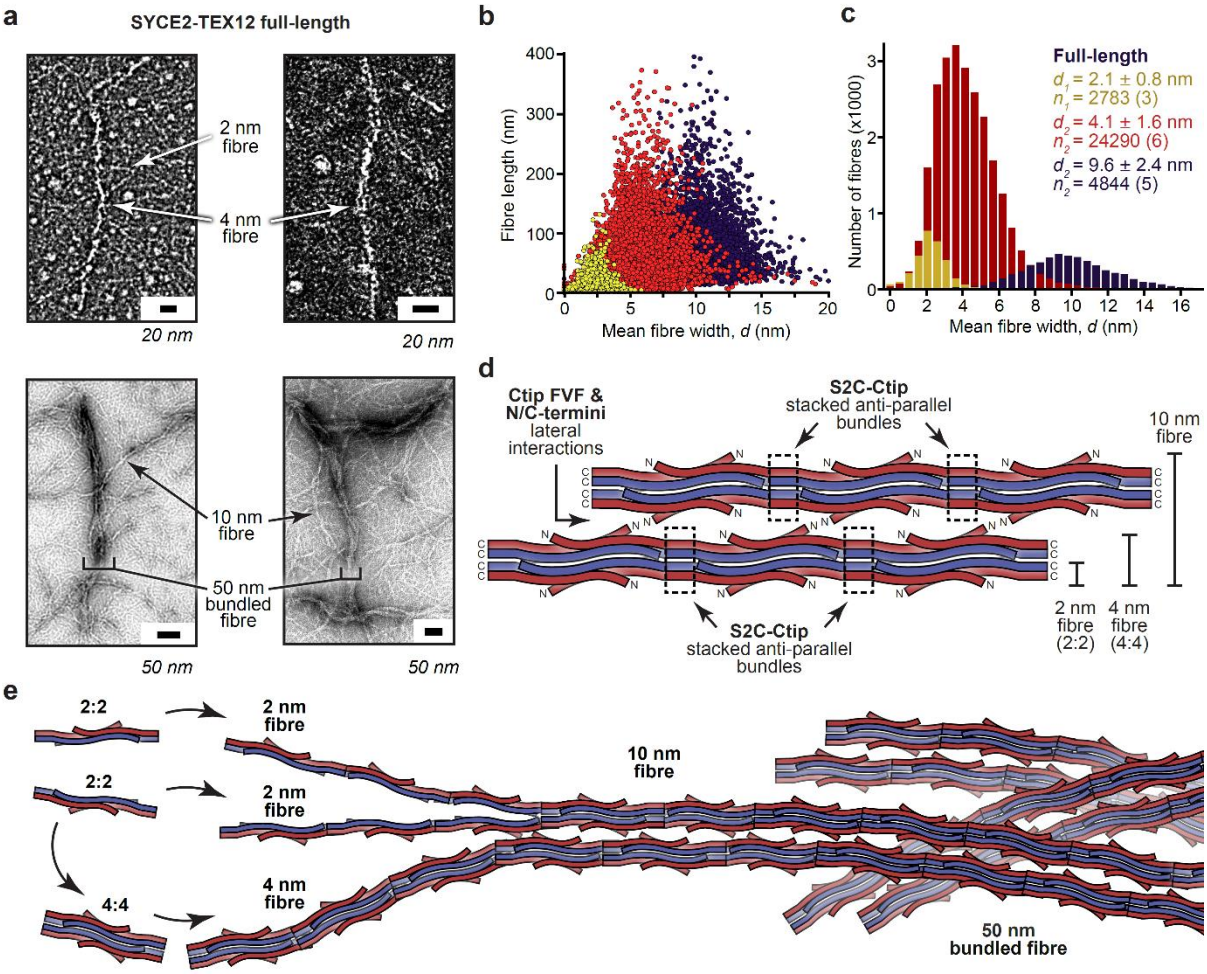


**Figure 8**

**A molecular mechanism for fibrous assembly of SYCE2-TEX12.**

(**a-c**) Electron microscopy of full-length SYCE2-TEX12 in which (**a**) electron micrographs reveal the presence of 2 nm, 4 nm and 10 nm fibres, which become intertwined in bundled fibres of up to 50 nm in width. (**b**) Scatter plots of mean fibre width (*d*, nm) against fibre length (nm), and (**c**) histograms of the number of fibres with mean widths within 0.5-nm bins, for three distinct populations (2 nm, yellow; 4 nm, red; 10 nm, blue). The mean, standard deviation and number of fibres in each population were determined from three, six and five micrographs, respectively. (**d**) Schematic of SYCE2-TEX12 fibrous assembly in which stacked S2C-Ctip anti-parallel bundles mediate back-to-back associations between subunits that generate 2 nm fibres and 4 nm fibres from 2:2 and 4:4 complexes, respectively. 10 nm fibres form through the lateral association of 4:4 fibres, mediated by Ctip FVF and N/C-terminal interactions. (**e**) Model of hierarchical fibrous assembly by SYCE2-TEX12. The building-block 2:2

complexes can assemble directly into 2 nm fibres, which then associate into 4 nm fibres, or can aggregate into ‘closed’ 4:4 structures that directly assemble into 4 nm fibres. The lateral association of 4 nm fibres generates 10 nm fibres, which become intertwined in bundled fibres of up to 50 nm width and many micrometres in length, and fulfil the known dimensions of the SC central element.

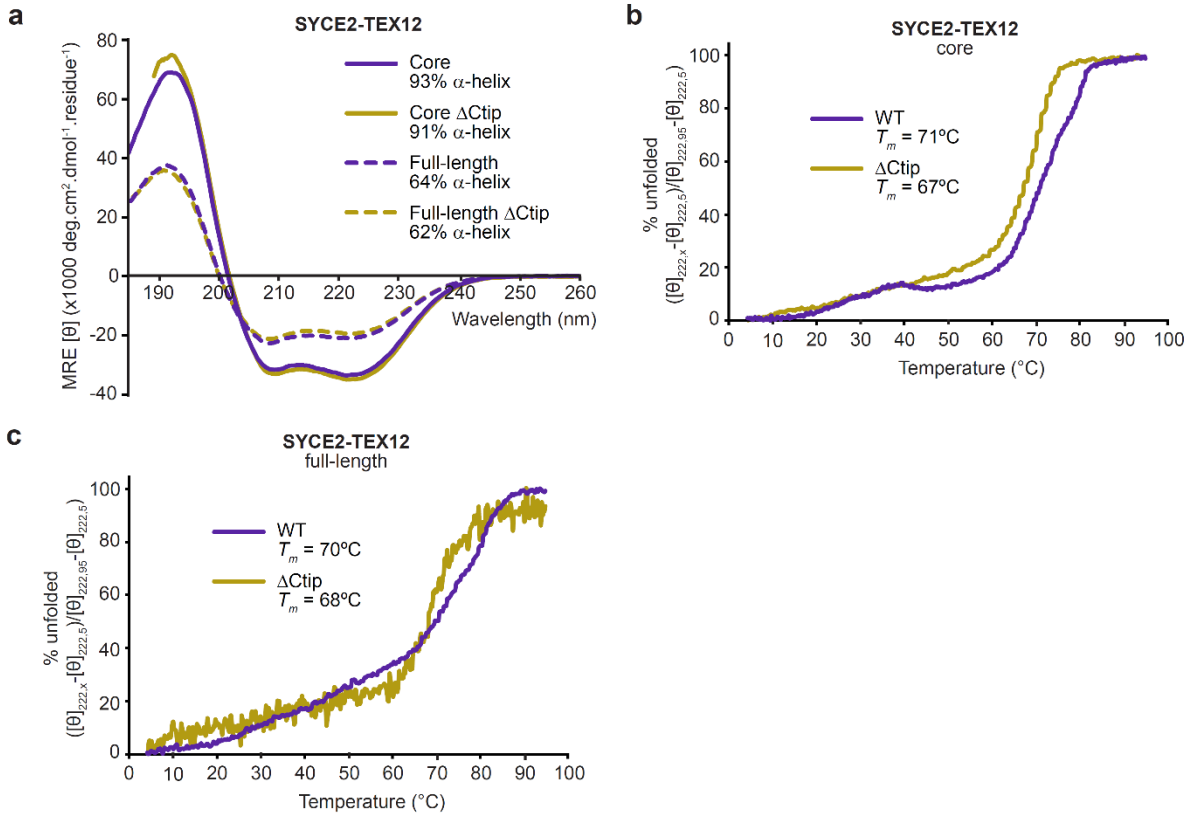


**Supplementary Figure 1**

**Circular dichroism analysis of SYCE2-TEX12 complexes.**

(**a-c**) Circular dichroism (CD) analysis of SYCE2-TEX12 core and full-length complexes containing wild-type (WT; purple) and ΔCtip (yellow) TEX12 sequences. (**a**) Far UV circular dichroism (CD) spectra recorded between 260 nm and 185 nm in mean residue ellipticity, MRE ([θ]) (x1000 deg.cm$^2$.dmol$^{-1}$.residue$^{-1}$). Data were deconvoluted using the CDSSTR algorithm, with helical content indicated. (**b-c**) CD thermal denaturation of SYCE2-TEX12 (**b**) core and (**c**) full-length complexes, recording the CD helical signature at 222 nm between 5°C and 95°C, as % unfolded. Melting temperatures were estimated, as indicated.

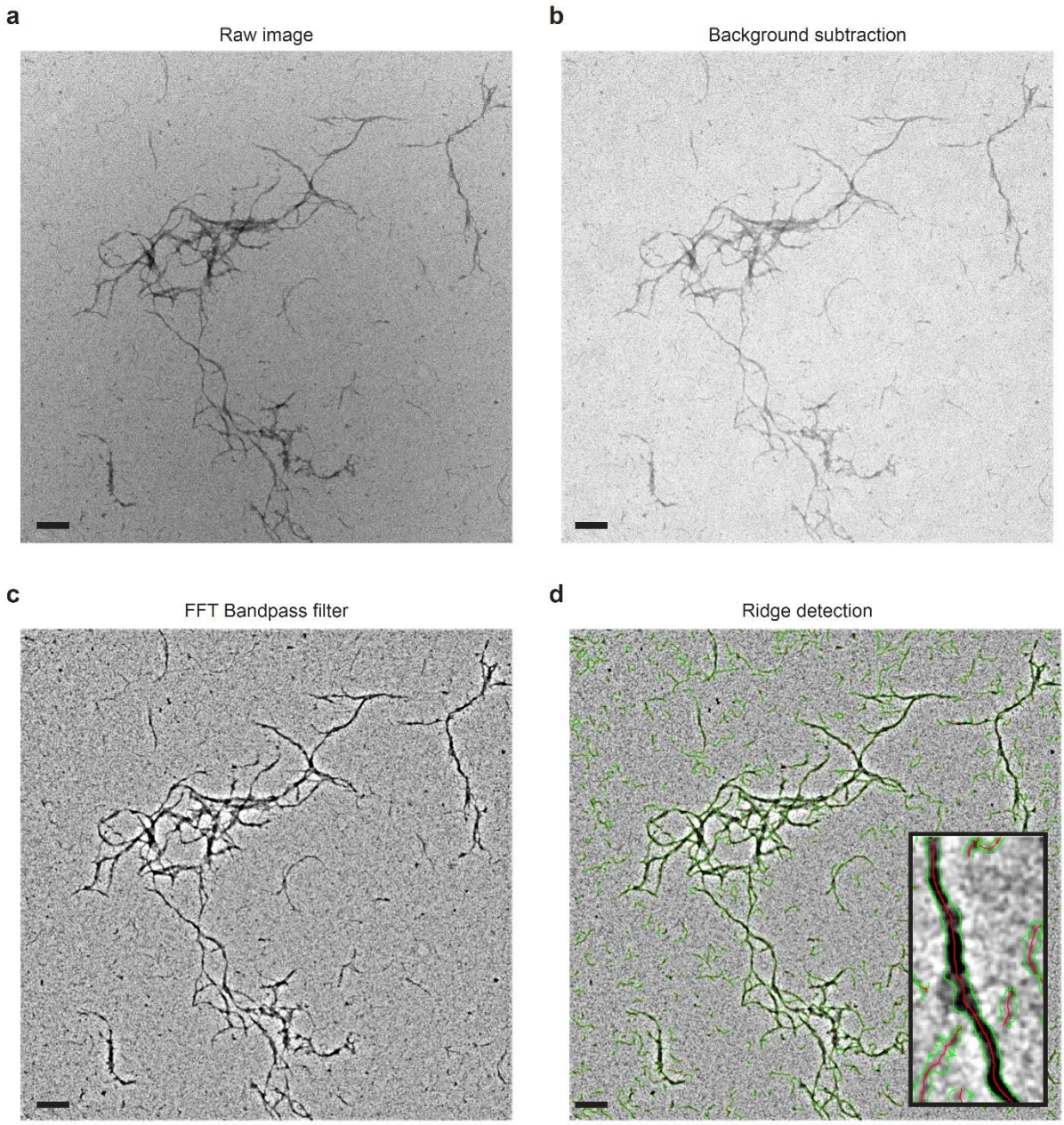


**Supplementary Figure 2**

**Image analysis of SYCE2-TEX12 electron micrographs.**

(**a-d**) The procedure used for automated image analysis and quantification of SYCE2-TEX12 fibres is shown for an example micrograph. The Fiji distribution of ImageJ was used to process (**a**) raw micrographs through (**b**) background subtraction and (**c**) FFT Bandpass filter. (**d**) Fibres were detected by the Ridge detection algorithm in which the centre and edges of interpreted fibres were highlighted in red and green, respectively, from which mean fibre widths and fibre lengths were determined.

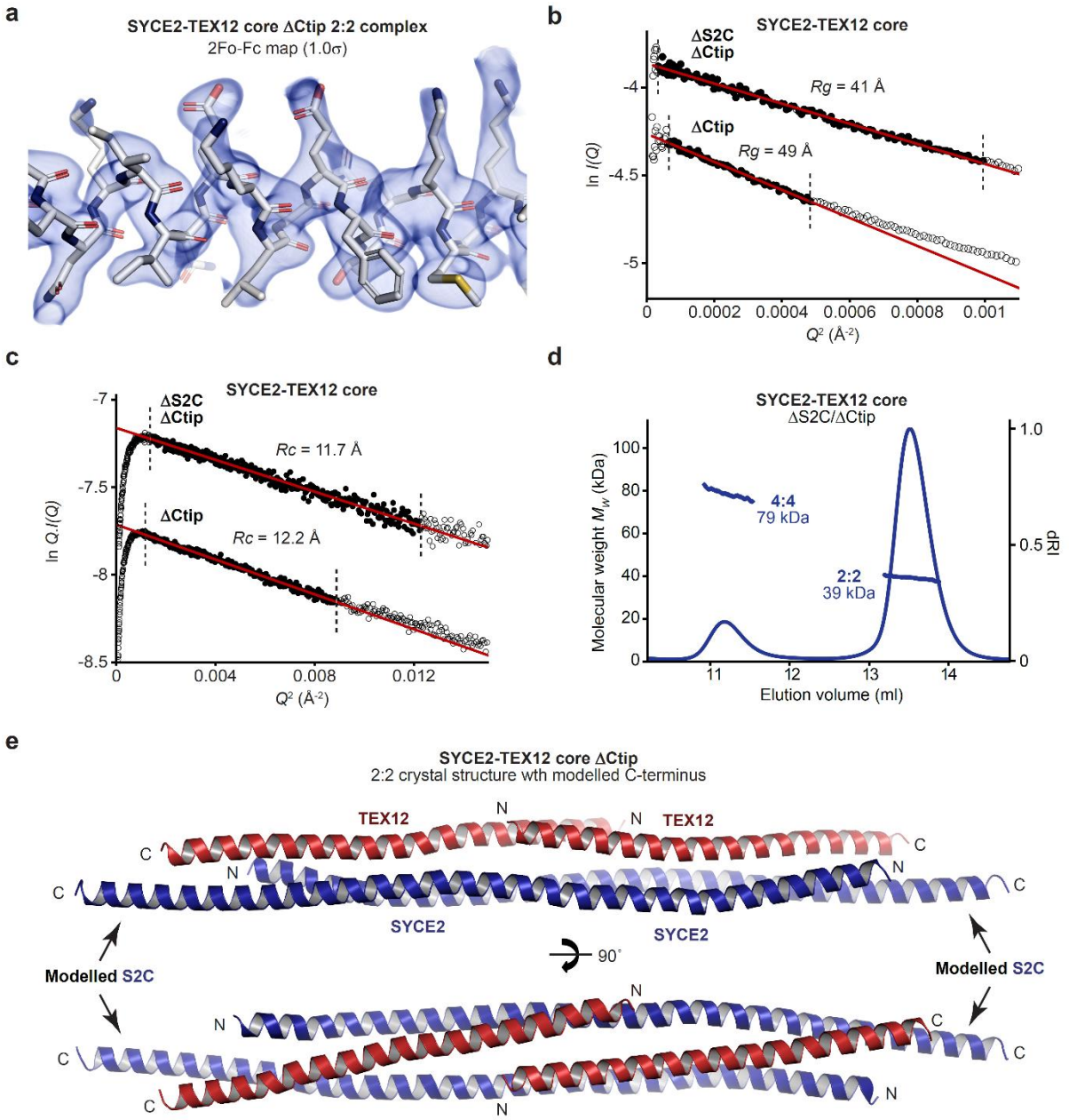


**Supplementary Figure 3**

**Crystal structure of the SYCE2-TEX12 core 2:2 complex.**

(**a**) 2Fo-Fc electron density map of the SYCE2-TEX12 core ΔCtip 2:2 complex (1.0σ) superimposed on the refined crystallographic model. (**b**) SEC-MALS analysis of SYCE2-TEX12 core ΔS2C/ΔCtip showing the formation of a 39 kDa 2:2 complex (86%; theoretical – 40 kDa) and a 79 kDa 4:4 complex (14%; theoretical – 79 kDa). (**c-d**) SEC-SAXS analysis of SYCE2-TEX12 core ΔS2C/ΔCtip. (**c**) SAXS Guinier analysis to determine the radius of gyration (*Rg*); linear fits are shown in red, with the fitted data range highlighted in black and demarcated by dashed lines. The *Q.Rg* values were < 1.3 and *Rg* was calculated

as 41 Å and 49 Å, respectively. (**d**) SAXS Guinier analysis to determine the radius of gyration of the cross-section (*Rc*); linear fits are shown in red, with the fitted data range highlighted in black and demarcated by dashed lines. The *Q.Rc* values were < 1.3 and *Rc* was calculated as 11.7 Å and 12.2 Å, respectively. (**e**) Theoretical model of the full SYCE2-TEX12 core ΔCtip 2:2 complex in which the missing C-terminal coiled-coil and S2C helix were docked onto the crystal structure.

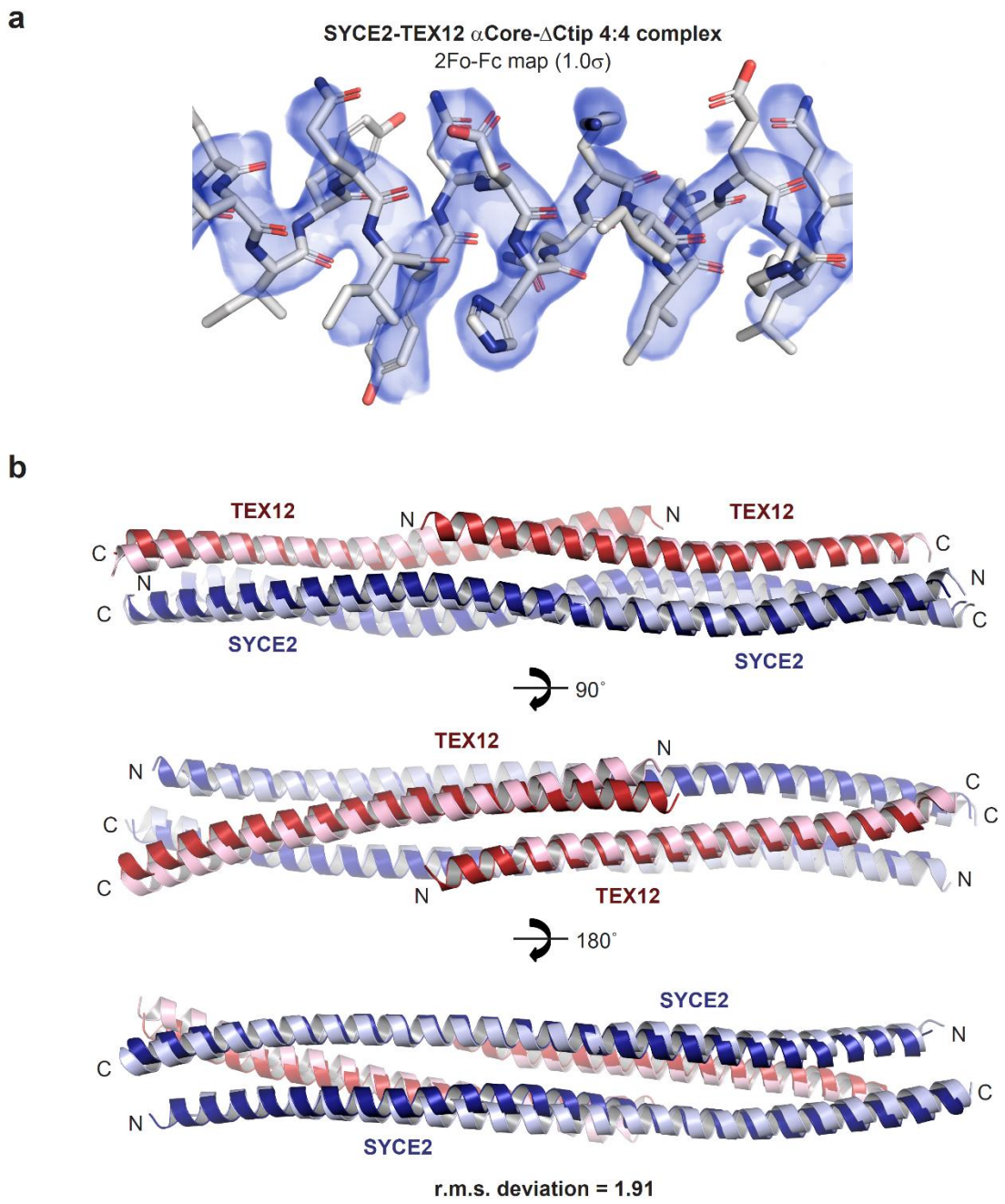


**Supplementary Figure 4**

**Crystal structure of the SYCE2-TEX12 core 4:4 complex.**

(**a**) 2Fo-Fc electron density map of the SYCE2-TEX12 core ΔCtip 4:4 complex (1.0σ) superimposed on the refined crystallographic model. (**b**) Superposition of a constituent 2:2 complex from the SYCE2-TEX12 core ΔCtip 4:4 structure (light blue and light red) and the SYCE2-TEX12 core ΔCtip 2:2 structure (dark blue and dark red), with r.m.s. deviation of 1.91.

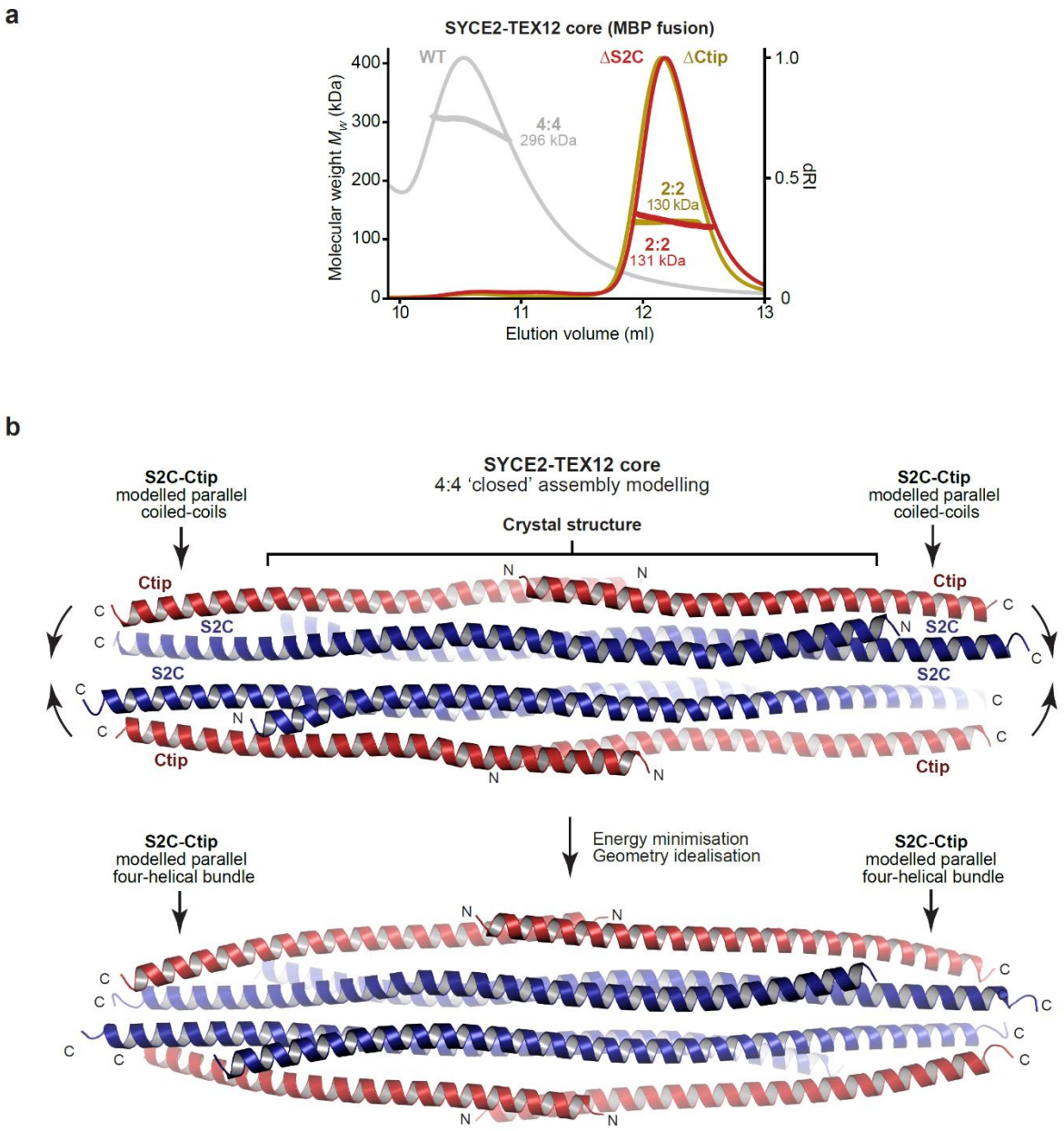


**Supplementary Figure 5**

**Modelling of the SYCE2-TEX12 core 'closed' 4:4 assembly.**

(**a**) SEC-MALS analysis of SYCE2-TEX12 core MBP-fusion proteins. SYCE2-TEX12 core wild-type is a 296 kDa 4:4 complex (theoretical – 278 kDa), whereas ΔS2C and ΔCtip form 131 kDa and 130 kDa 2:2 complexes, respectively (theoretical – 136 kDa and 137 kDa. (**b**) Modelling of the 'closed' 4:4 assembly. Theoretical S2C-Ctip hetero-dimeric coiled-coils were docked onto the 4:4 crystal structure (top) and allowed to form C-terminal S2C-Ctip four-helical bundles through iterative energy minimisation and geometry idealisation (bottom).

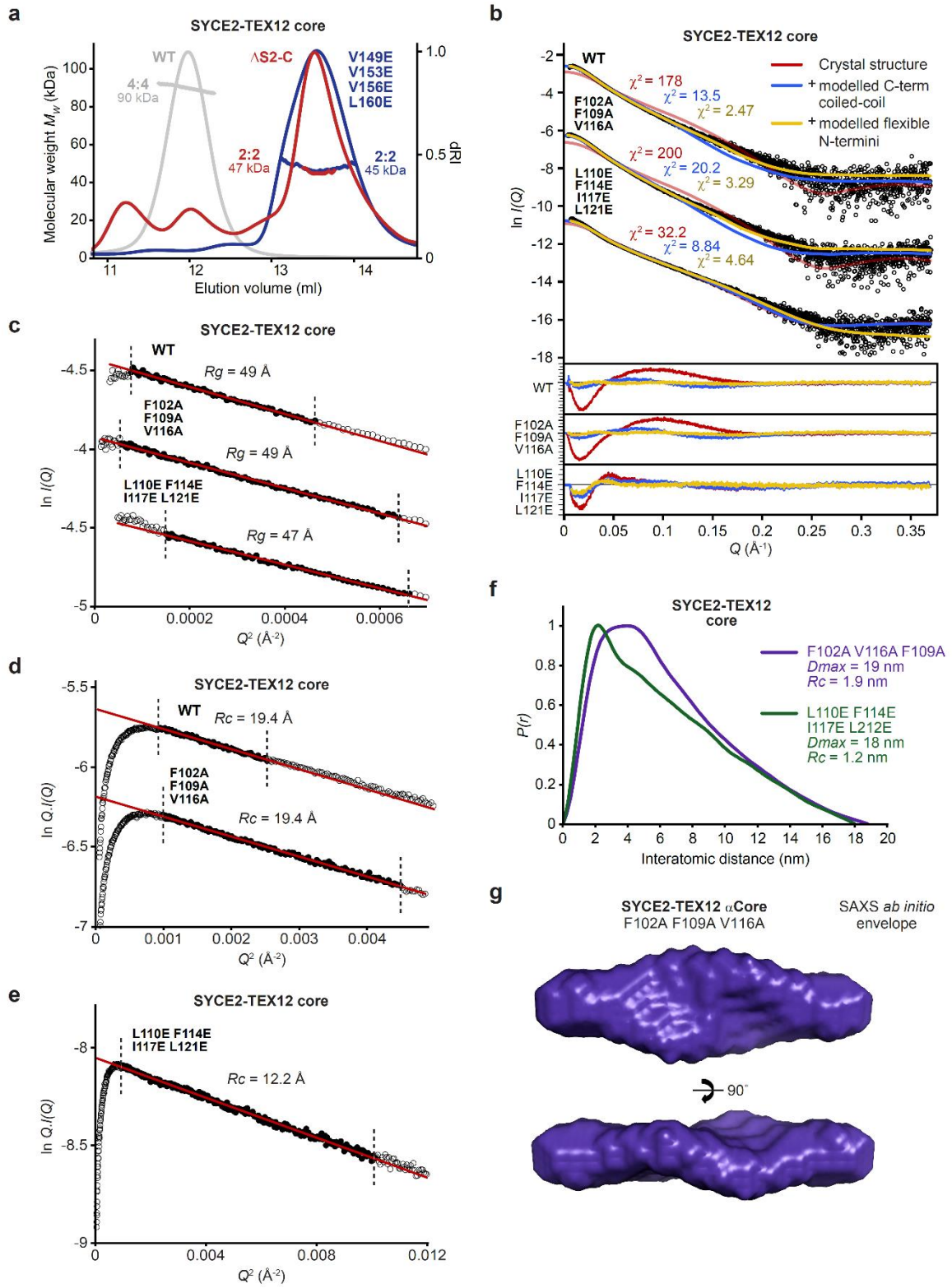


**Supplementary Figure 6**

**MALS and SAXS analysis of SYCE2-TEX12 wild-type and mutant complexes.**

(**a**) SEC-MALS analysis of SYCE2-TEX12 core ΔS2C and V149E, V153E, V156E and L160E mutants, demonstrating the formation of 47 kDa and 45 kDa 2:2 complexes, respectively (theoretical – 42 kDa

and 45 kDa). The wild-type 90 kDa 4:4 complex is shown in grey for comparison. (**b-g**) SEC-SAXS analysis of SYCE2-TEX12 core wild-type, F102A F109A V116A (FFV) and L110E F114E I117E L121E (LFIL) mutants. (**b**) SAXS scattering data overlaid with the theoretical scattering curves of the 4:4 crystal structure (red), with modelled Ctip-S2C C-terminal bundles (blue), and with flexibly modelled N-termini (yellow); $\chi^2$ values are indicated and residuals for each fit are shown (inset). (**c**) SAXS Guinier analysis to determine the radius of gyration (*Rg*); linear fits are shown in red, with the fitted data range highlighted in black and demarcated by dashed lines. The *Q.Rg* values were < 1.3 and *Rg* was calculated as 49 Å, 49 Å and 47 Å, respectively. (**d-e**) SAXS Guinier analysis to determine the radius of gyration of the cross-section (*Rc*); linear fits are shown in red, with the fitted data range highlighted in black and demarcated by dashed lines. The *Q.Rc* values were < 1.3 and *Rc* was calculated as (**d**) 19.4 Å for wild-type and FFV and (**e**) 12.2 Å for LFIL. (**f**) SAXS *P(r)* interatomic distance distributions of SYCE2-TEX12 core FFV and LFIL, showing maximum dimensions of 19 nm and 18 nm, respectively. (**g**) SAXS *ab initio* model of SYCE2-TEX12 core FFV in which a filtered averaged model from 30 independent DAMMIF runs is shown.

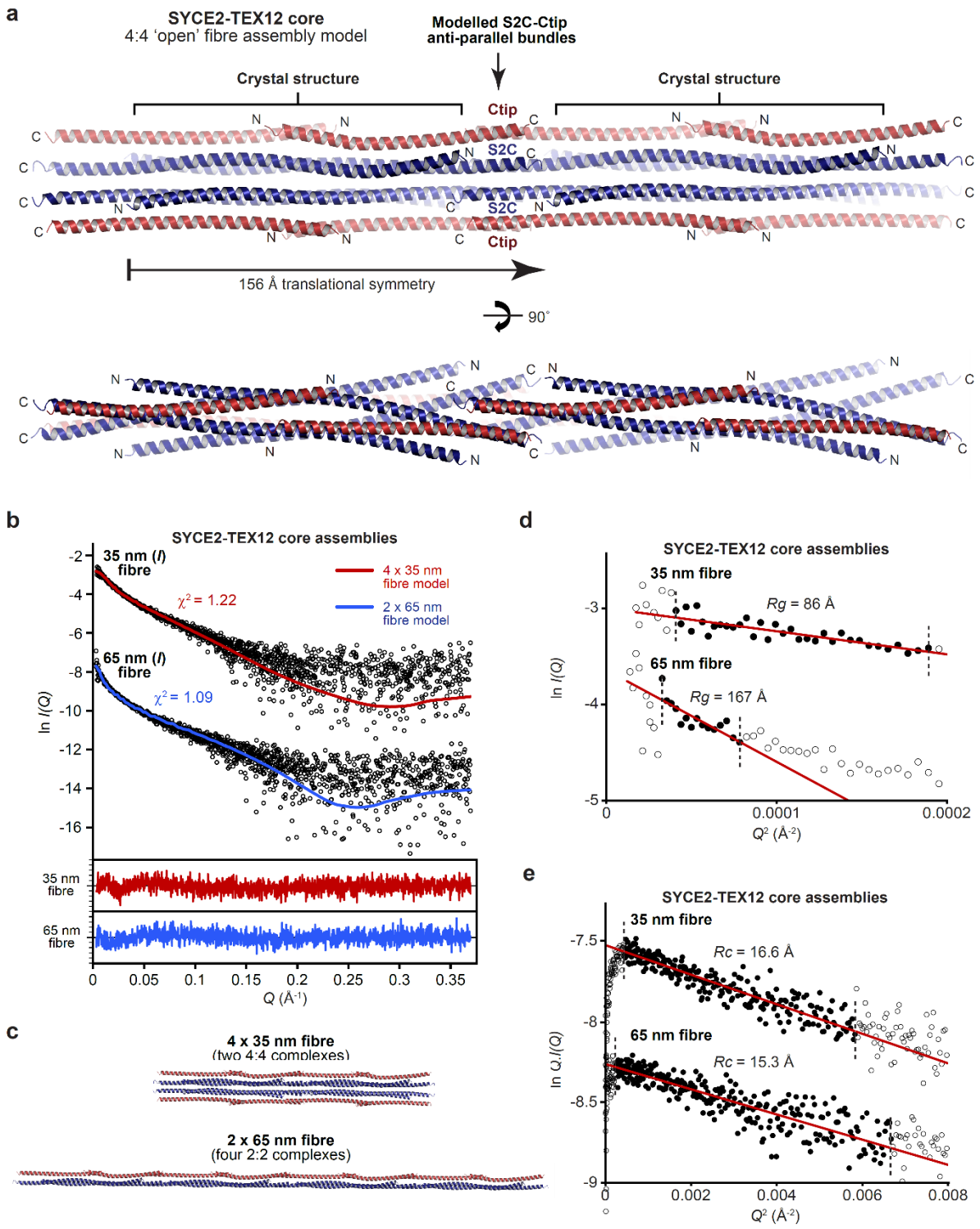


**Supplementary Figure 7**

**Modelling of the SYCE2-TEX12 core fibrous assembly.**

(**a**) Model of SYCE2-TEX12 core fibrous assembly in which adjacent 4:4 complexes are translated by 15 nm and interact back-to-back through stacked S2C-Ctip anti-parallel four-helical bundles. (**b-e**) SEC-

SAXS analysis of SYCE2-TEX12 core 35 nm and 65 nm (length) fibres. (**b**) SAXS scattering data overlaid with the theoretical scattering curves of a 4 x 35 nm (w x l) fibre model (two consecutive 4:4 complexes, red) and a 2 x 65 nm (w x l) fibre model (four consecutive 2:2 complexes, blue); $\chi^2$ values are indicated and residuals for each fit are shown (inset). (**c**) The 4 x 35 nm and 2 x 65 nm fibre models used for SAXS data fitting. (**d**) SAXS Guinier analysis to determine the radius of gyration (*Rg*); linear fits are shown in red, with the fitted data range highlighted in black and demarcated by dashed lines. The *Q*.*Rg* values were < 1.3 and *Rg* was calculated as 86 Å and 167 Å, respectively. (**e**) SAXS Guinier analysis to determine the radius of gyration of the cross-section (*Rc*); linear fits are shown in red, with the fitted data range highlighted in black and demarcated by dashed lines. The *Q*.*Rc* values were < 1.3 and *Rc* was calculated as 16.6 Å and 15.3 Å, respectively.